Development of Active Magnetic Shielding for the Neutron Electric Dipole Moment Experiment at TRIUMF

By

Michael Loren Lang

A Thesis submitted to the Faculty of Graduate Studies of
The University of Manitoba
in partial fulfillment of the requirements for the degree of

MASTER OF SCIENCE

Department of Physics and Astronomy
University of Manitoba
Winnipeg

Acknowledgments

I would like to thank my advisor Chris Bidinosti, for his help and support during graduate studies. I would also like to thank David Ostapchuk and Troy Dawson for their conversation and assistance around the lab during the course of my research.

Abstract

Next generation electric dipole moment experiments require a high level of magnetic field stability in the experimental volume. Active magnetic shielding has been proposed to provide low-frequency magnetic field stability in the neutron electric dipole moment (nEDM) experiment planned for TRIUMF. A prototype active magnetic shielding system was constructed and tested at the University of Winnipeg. The system is capable of providing RMS shielding factors > 1000 for magnetic field perturbation frequencies ≤ 20 mHz, and > 100 for frequencies ≤ 0.5 Hz, and can reduce magnetic field variations on the order of tens of μT to the level of tens of nT. The achievable shielding factor was limited by the field sampling rate limit of $\sim$400 Hz, and by the background field noise floor of the laboratory. This represents good progress towards the eventual system for nEDM experiments, where low-frequency field drifts on the order of 100 nT require active shielding to the order of 1 nT.

Contents

List of Figures

List of Tables

Chapter 1

Introduction

The Standard Model of particle physics is a theory describing the fundamental particles of matter and their interactions. The fundamental particles come in two varieties: fermions, which are the principle building blocks of matter, and bosons, which are the carriers of the strong, weak, and electromagnetic forces, responsible for mediating the dynamics of known subatomic particles. The Standard Model is strongly supported by experimental evidence, however, it fails to account for the observed baryon asymmetry of the present-day universe (excess of matter over antimatter). Current predictions of CP violation (violation of invariance under the combined charge conjugation (C) and parity (P) operators) in the Standard Model are considered too small to account for the baryon asymmetry. New theories describe CP violating processes that go beyond the predictions of the Standard Model. These theories are the driving force behind experimental searches for new sources of CP violation, which includes the search for non-zero electric dipole moments (EDMs) of certain particles. The focus of this thesis is the development and testing of an active magnetic shielding system intended to support an experiment at TRIUMF (Canada's National Laboratory for Particle Nuclear Physics, Vancouver, BC), searching for a non-zero neutron electric dipole moment (nEDM).

1.1 The neutron

The neutron, which has the symbol n, is a spin-half hadron composed of one up quark and two down quarks. This quark combination results in a zero net electric charge on the neutron. Neutrons

are one of the two nucleons (protons being the other) which make up the nuclei of atoms. Neutrons are bound in nuclei by the strong nuclear force. The binding is typically in the MeV scale. To free neutrons, a nuclear reaction is required. Free neutrons are unstable with a lifetime of 880.0 ± 0.9 s. The neutron mass is 939.565379 ± 0.000021 MeV [5, 10].

1.2 CP violation and the search for the neutron electric dipole moment

Under the assumption of Lorentz symmetry, the simultaneous transformation of charge conjugation, parity conjugation, and time-reversal (CPT) leaves all SM interactions unchanged [11, 19]. This implies that a time-reversal (T) violating process can also be considered a CP-violating process. Existence of non-zero EDMs implies a violation of time reversal invariance and is therefore an excellent probe of CP-violation [13]. To understand how the violation of T-symmetry occurs, consider a particle of spin $\vec{S}$ within an electric and magnetic field, $\vec{E}$ and $\vec{B}$ respectively. The Hamiltonian for such a particle is

$$H = -\mu \vec{B} \cdot \frac{\vec{S}}{S} - d\vec{E} \cdot \frac{\vec{S}}{S}, \tag{1.1}$$

where μ is the magnetic moment and d is the electric dipole moment [34]. Under time reversal the magnetic field contribution remains unchanged, $T(\vec{B} \cdot \vec{S}) = \vec{B} \cdot \vec{S}$, whereas the electric field contribution picks up a negative sign, $T(\vec{E} \cdot \vec{S}) = -\vec{E} \cdot \vec{S}$. A non-zero EDM will violate T-symmetry, and therefore CP-symmetry as well.

The Standard Model of particle physics provides only two separate sources of CP violation. The first source is established by the strong interaction, described by the θ-term of the quantum chromodynamics (QCD) Lagrangian [45]. The θ-term is the lowest order operator of the QCD Lagrangian, and is a CP-violating, dimension four term involving the gluon field. The θ-term, described by a dimensionless coupling θ, is flavor-diagonal and induces a neutron EDM of $|d_n| \approx \theta \times 3 \cdot 10^{-16}$ e·cm [25]. The current best experimental upper limit on the neutron EDM is $|d_n| <$

2.9×10^{-26} e·cm, which is well below the prediction of QCD unless θ is extremely small. The reason for the smallness of θ is currently unknown, which suggests a fine tuning issue and is known as the strong-CP problem. As a result of this, it is assumed that θ is zero or almost disappears due to a symmetry or possibly a dynamic mechanism [31].

The second source of CP violation in the SM is found in the electroweak sector, and derives from the irreducible phase in the Cabibbo-Kobayashi-Maskawa (CKM) matrix [25]. CP violation within the CKM matrix places the neutron EDM in the range of $|d_n| = 10^{-31} - 10^{-32}$ e·cm, well below the current best experimental limit stated above.

If the neutron EDM is found to be larger than the prediction, it could signify new physics beyond the Standard Model. One of the great unanswered questions in physics is why there exists a baryon asymmetry in our present-day universe. This predominance of matter over antimatter is strongly correlated to the observation of a non-zero neutron EDM, making it an excellent candidate for experimentation.

1.3 Electroweak baryogenesis

One of the fundamental problems in cosmology is the existence of an excess of matter over antimatter in the modern universe. This is called the baryon asymmetry of the universe (BAU). It is believed that in the early universe, the net baryon number must initially have been zero [27, 34]. The explanation of the origin and evolution of the BAU is known as baryogenesis. The BAU and baryogenesis cannot be explained by the standard model (SM). The inability of the SM to explain baryogenesis is considered to be one of the strongest indications of the incompleteness of the SM [12].

In order to generate the BAU, particle physics models must meet certain criteria. The set of three criteria are known as the Sakharov conditions [8, 12, 27, 41]:

1. There must be a violation of baryon number B conservation, otherwise the net baryon number of the universe would not change over time.

2. Violation of C (charge conjugation symmetry) and CP (the product of charge conjugation

symmetry and parity) must be present to create inequality between rates of $\Delta B \neq 0$ processes. This ensures asymmetry in the creation of baryon and anti-baryon quantities in the development of the early universe.

3. At thermal equilibrium the average baryon amount would be constant and an equal amount of baryons and antibaryons would be present, therefore a departure from thermal equilibrium must take place to evolve net baryon number over time.

The BAU remains unsolved to this day, however, theories of new physics have been developed to explain the phenomenon. An example of such a theory is electroweak baryogenesis (EWBG), which attempts to explain the baryon asymmetry using electroweak (EW) theory combined with new physics at the TeV scale [27].

In electroweak baryogenesis, a first-order electroweak phase transition is required. As the universe cools, this results in the formation of bubbles of the broken electroweak phase within the surrounding plasma of the symmetric phase (as illustrated in Figure 1.1). The expanding bubbles induce a departure from thermal equilibrium and thereby satisfy condition 3. In the symmetric

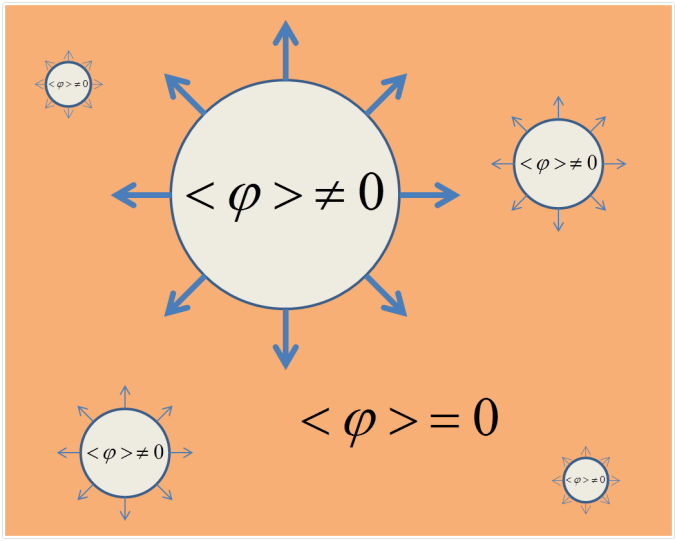

Figure 1.1: First order phase transition in electroweak baryogenesis. Bubbles of broken phase ($\langle\phi\rangle \neq 0$) expand within the surrounding symmetric phase plasma ($\langle\phi\rangle = 0$). The order parameter $\langle\phi\rangle$ is related to the vacuum expectation value of the Higgs field.

phase outside the bubbles, rapid baryon-number violating processes occur, which satisfy condition 1. These are called sphaleron transitions. A sphaleron is a static, unstable solution to the

electroweak theory. The sphaleron process is allowed in the SM, in the symmetric (unbroken) electroweak phase. It is effectively a process by which baryon number is converted to lepton number in steps of three, as illustrated in Figure 1.2 (inset). The sphaleron transitions are strongly suppressed in the broken phase. Therefore, as the universe cools and bubble expansion occurs, any net baryon number created in the symmetric phase would be pulled into the broken phase environment of the bubble, where it is effectively locked (as also illustrated in Figure 1.2). However, since forward and reverse sphaleron transitions occur, and since they can generate both positive and negative baryon number, no net baryon number would be accrued unless C- and CP-violating processes would occur.

It is therefore C- and CP-violating processes, that occur near the phase boundary of the bubble wall, which create particle number asymmetries that produce more baryons than antibaryons. This satisfies condition 2, and results in an evolution of net nonzero baryon number in time. Eventually, the universe cools sufficiently that the expanding bubbles coalesce into a homogeneous universe containing only the broken EW phase, and the final net baryon number is locked in.

In order for EW baryogenesis to generate the correct magnitude of the observed baryon asymmetry, it was realized that additional CP-violation beyond the SM would be required [27, 28]. New sources of CP-violation have therefore been proposed in order to solve this issue. The models often introduce new particles near the TeV scale which possess CP-violating interactions. Calculations have been conducted in the framework of supersymmetry, where additional CP-violating interactions may be permitted [34]. Generally, it is believed that new physics at the TeV scale is a natural way to make EW baryogenesis correctly predict the BAU, supersymmetry being one example of this [27].

While the theories that go beyond the SM provide an explanation for the BAU, experimental evidence is required to test them. A search for a non-zero EDM is a promising way to search for new sources of CP violation.

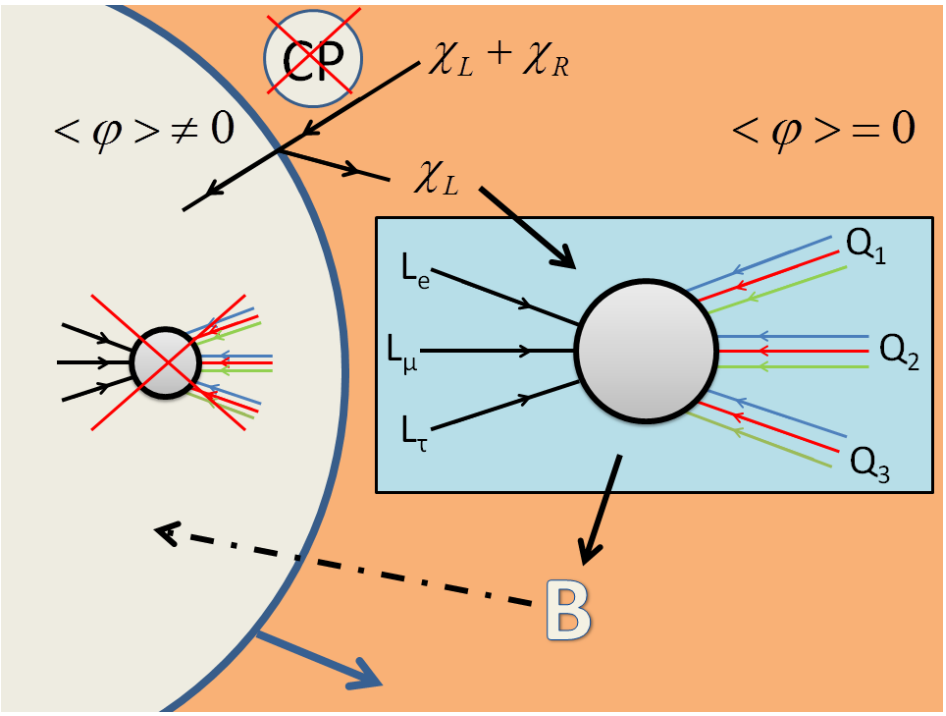

Figure 1.2: Sphaleron process (inset) occurs for left-handed fermions χ_L in the symmetric phase ($\langle\phi\rangle = 0$) region. This converts leptons $L_{e,\mu,\tau}$ to quarks $Q_{1,2,3}$ thereby creating a net baryon charge B, which is drawn into the expanding bubble. Within the bubble, the phase is broken ($\langle\phi\rangle \neq 0$) and the sphaleron process is suppressed. CP violation is also required so that the same process does not occur for anti-particles at the same rate.

1.4 The use of UCN in an EDM experiment

Neutrons with energies $\lesssim 300$ neV are known as ultracold neutrons (UCN). UCN energies are low enough that they undergo total reflection at any angle of incidence off material walls, and therefore, they may be trapped in material bottles for extended periods of time. The ability to trap UCN results from their interaction with the fermi potential of the material walls via the strong force, and the storage time is limited by the free neutron decay via the weak force. The mean lifetime of a neutron is $\tau_n = 881.5$ s, providing a long time frame for experimentation.

Under the influence of a magnetic field B, a neutron spin will precess at the Larmor frequency $\omega = \gamma B$, where γ is the gyromagnetic ratio. A neutron EDM is typically measured by observing the Larmor frequency of UCN in aligned magnetic and electric fields. If the fields are parallel,

$$\hbar\omega_0^{\uparrow\uparrow} = |2\mu_n B + 2d_n E|, \tag{1.2}$$

where $\hbar$ is the reduced Planck constant, $\omega_0^{\uparrow\uparrow}$ is the Larmor frequency for parallel B-, and E-fields, μ_n is the magnetic moment of the neutron, d_n is the electric dipole of the neutron, and E is the electric field magnitude. For a reversal of the electric field direction,

$$\hbar\omega_0^{\uparrow\downarrow} = |2\mu_n B - 2d_n E|, \tag{1.3}$$

where $\omega_0^{\uparrow\downarrow}$ is the Larmor frequency for anti-parallel fields resulting from the E-field being reversed. Thus the neutron EDM may be extracted by comparing the two configurations:

$$d_n = \frac{\hbar\left(\omega_0^{\uparrow\uparrow} - \omega_0^{\uparrow\downarrow}\right)}{4E}. \tag{1.4}$$

1.5 ILL UCN-EDM experiment

The best experimental measurement of the neutron EDM gave $d_n < 2.9 \times 10^{-26}$ e·cm at 90% confidence level [2]. The experiment was performed at the Institut Laue-Langevin (ILL) in Genoble, France. The precision of the result was limited by statistics. The UCN density in the EDM cell (21 L) was 0.7 UCN/cm^3.

The experimental setup used at ILL is described in Figure 1.3. UCN production at ILL is achieved by a rotor source used to down-scatter cold neutrons [35]. Polarized UCN are transported into the experimental volume. Uniform magnetic and electric fields, oriented either parallel or anti-parallel to one another, are applied within the experimental volume. For each orientation of the applied fields, the precession frequency ω_0 of the neutrons is measured.

Measurement of the UCN precession frequency in this experiment is performed using a technique known as the Ramsey separated oscillatory field magnetic resonance method, or Ramsey resonance, for short [36,37]. UCN are spin-polarized by transmission through a thin, magnetized iron foil, and then transported into the measurement volume. The UCN are stored in the measurement volume with their spins aligned with a vertical magnetic field B_0. Perpendicular to B_0, a uniform oscillating field of amplitude B_1 and frequency ω is applied to the UCN for a time τ. This is an RF pulse

known as a $\frac{\pi}{2}$-pulse, because it deflects the vertically aligned spins into the horizontal plane. The B_1 field is then switched off and the spins are allowed to precess freely in the horizontal plane at the Larmor frequency $\omega_0 = \gamma B_0$ (ignoring the effect of the electric field) for a time T. Another $\frac{\pi}{2}$ pulse of the same phase as the first is applied, and the UCN are drained from the measurement cell. If the RF pulses are in phase with the neutron spin precession, the result is a rotation in the neutron spins by 180°. RF pulses of slightly different frequencies will cause the resulting direction of the neutron spins to vary according to the phase difference between the RF and the neutron precession. As the neutrons leave the cell they fall down onto the polarizing foil which acts as a spin analyzer. The neutrons in the initial spin state pass through the foil into a detector to be counted. An rf magnetic field is applied above the polarizing foil which flips the spin of the remaining neutrons, allowing them to pass through the foil for counting [2]. Depending on the frequency ω of the applied B_1 field, the number of UCN counts will vary. This is seen in an oscillating pattern of the UCN counts, which reflects the phase difference between the applied B_1 field and the neutron precession. The central minimum, in counts, represents the resonant frequency ω_0 of the neutrons. As described in the previous section, the electric dipole moment of the neutron d_n can be determined using Equation 1.4.

The uncertainty σ_{d_n} on the measurement due to neutron counting statistics is

$$\sigma_{d_n} = \frac{\hbar}{2\alpha E T\sqrt{N}}, \tag{1.5}$$

where α is the polarization product (related to the polarization of the neutrons after leaving the measurement cell), E is the strength of the electric field, T is the length of free precession time between the RF pulses, and N is the total number of neutrons counted. The ILL experiment typically achieved $\alpha = 0.64$, $T = 130\ s$, $E = 10$ kV/cm, and $N = 14,000$ UCN/edm cycle, where a cycle took 215 s [3]. Using these parameters the measurement sensitivity was:

$$\sigma_{d_n} = 17 \times 10^{-26}\ e \cdot \text{cm/day} \tag{1.6}$$

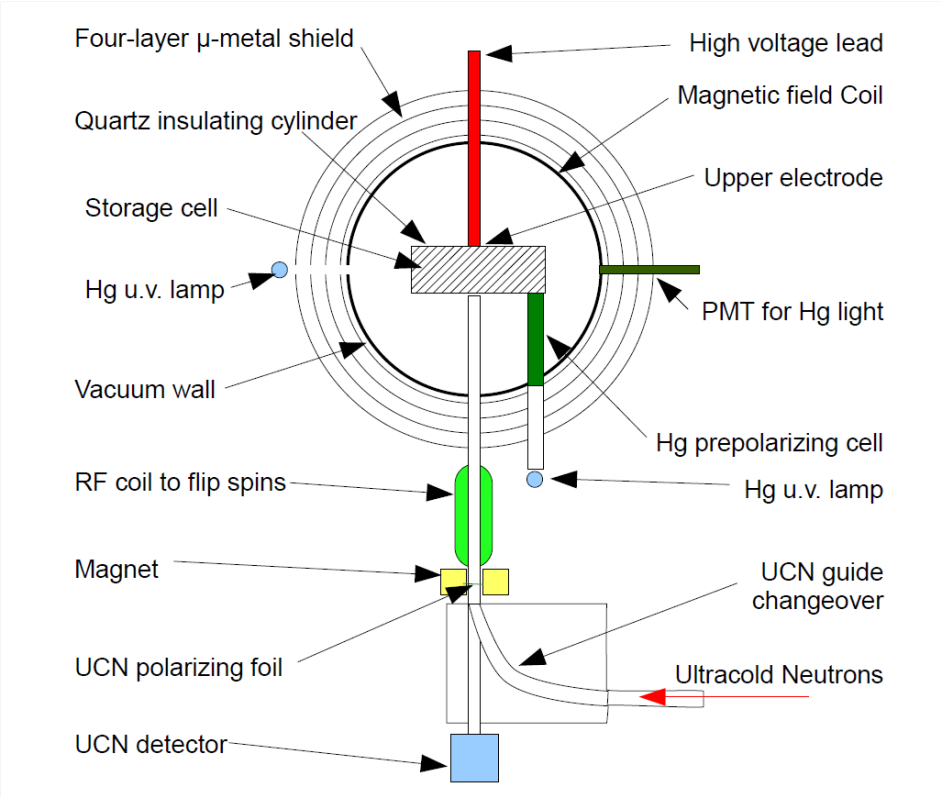

Figure 1.3: Experimental setup used at the ILL to achieve the present best experimental limit of the neutron EDM [2]. UCN enter the apparatus at the bottom right and pass through a polarizing foil to ensure the those transported to the storage cell are nearly fully polarized. The neutrons in the cell are aligned with the interior magnetic field of 1 μT, and a DC electric field of 12 kV/cm is applied along the direction of the magnetic field. B_1 field pulses are applied and the neutron precession frequency is measured using Ramsey's method. Once the sequence is completed, the cell door is opened allowing the neutrons to leak out into a neutron detector, first passing through the polarizing foil which is now used as a spin analyzer. The Hg components shown are used for the Hg-199 comagnetometer, which provides an accurate measure of the fields used in the experiment.

Small drifts in the B_0 fields ($\sim$ tens of pT) produce shifts in the neutron precession frequency, obscuring the possible effect of a non-zero d_n. To correct for these changes, an Hg-199 comagnetometer is used to perform a simultaneous measurement of the magnetic field in the neutron storage cell. The Hg-199 is polarized by optical pumping prior to being transported into the cell with the neutrons. As with the UCN, the mercury spins are rotated into the perpendicular plane using magnetic resonance. The spin precession is monitored using a circularly polarized beam of 254 nm resonance radiation which is subject to an absorption proportional to the transverse component of the Hg spin vector. The frequency is measured by detecting the change in optical signal of a photomultiplier tube measuring the incident beam [15].

Using the mercury comagnetometer, the drift in magnetic field within the cell for a single batch was measurement to about 200 fT [15]. That may be compared to the ∼1 pT uncertainty in the neutron measurement due to counting statistics. The higher precision drift measurement of the comagnetometer represented a significant correction to the raw neutron precession data. The results of the correction can be seen in Ref. [15], where the impact of the B-field drift on the neutron precession is reduced below the level of the statistical uncertainty σ_{d_n}.

The ILL experimental setup also used passive magnetic shielding to reduce background fields in the experimental region. The shielding system was composed of four concentric μ-metal cylinders, as shown in Figure 1.3. The shields had endcaps, as well as several other protrusions for access and services.

1.6 Proposed UCN EDM experiment at TRIUMF

TRIUMF will soon house a new high density UCN source, presently being developed at the Research Center for Nuclear Physics (RCNP) in Osaka, Japan. The source works by liberating neutrons from a spallation target by an incident proton beam. The neutrons are cooled down by room temperature and 10K-D_2O moderators to become cold neutrons prior to becoming UCN via downscattering (phonon production) in a bath of superfluid He at 0.8 K. Compared with the UCN source at ILL which achieved 0.7 UCN/cm^3 in the EDM cell, the UCN source at TRIUMF is expected to deliver 1200 polarized UCN/cm^3 to the experimental cell [26], which will significantly reduce the statistical error related to the total number of neutrons measured per cycle of the experiment. This expectation is attributed to the combination of the spallation source and the use of superfluid helium for production of UCN, features unique to the TRIUMF strategy.

As previously mentioned, the precession frequency ω of the neutron within a magnetic and electric field is

$$\hbar\omega = 2\mu B_0 \pm 2d_n E, \tag{1.7}$$

This thesis concerns the stability of B_0 with time. If B_0 is unstable, it could represent a significant additional random error, which we will call a systematic error. The term statistical error is reserved

to refer to the fundamental goal statistical error relating to the neutron counting statistics. Considering the statistical error component, the neutron counting statistics results in a statistical error on the neutron EDM per cycle δd_n which can also be written as a statistical error on the precession frequency of the neutrons:

$$\hbar\,\delta\omega_{stat} = 2(\delta d_n)E\ , \tag{1.8}$$

where δd_n is expected to be $\sim 1\times10^{-25}$ e·cm per cycle [32]. Using a value of 10 kV/cm for E, $\delta\omega_{stat}$ can be calculated as follows:

$$\delta\omega_{stat} = \frac{2(10^{-25}\ e\cdot\mathrm{cm})(10\ \mathrm{kV/cm})}{1.05\times10^{-34}\ J\cdot\mathrm{s}}\cdot\frac{10^3\ \mathrm{V}}{\mathrm{kV}}\cdot\frac{1.6\times10^{-19}\ \mathrm{J}}{e\mathrm{V}} \tag{1.9}$$

$$= 3.05\times10^{-6}\ \mathrm{rad/s} \tag{1.10}$$

$$\Rightarrow \delta f = 4.85\times10^{-7}\ \mathrm{Hz} = 485\ \mathrm{nHz}\ , \tag{1.11}$$

where $\delta f = \delta\omega/(2\pi)$ is the precesion in linear frequency.

The magnetic field stability requirement can then be calculated by requiring that its stability be, at worst, equivalent to this precision:

$$\delta\omega = \gamma\delta B_0\ , \tag{1.12}$$

where γ is the gyromagnetic ratio ($\gamma\!\!\!^{-} \equiv \gamma/(2\pi) \simeq 30$ Hz/μT for neutrons). The required precision on the magnetic field δB_0 may then be obtained as

$$\delta B_0 = \delta f/\gamma\!\!\!^{-}\ . \tag{1.13}$$

Inserting the values for δf and $\gamma\!\!\!^{-}$ gives

$$\delta B_0 = \frac{4.85\times10^{-7}\ \mathrm{Hz}}{30\ \mathrm{Hz}/\mu\mathrm{T}} = 16.2\ \mathrm{fT}\,. \tag{1.14}$$

The magnetic stability requirement is then ~ 16 fT averaged over one cycle of the experiment.

Each cycle (four neutron fills of the cell) is expected to take 43 minutes [32]. This places a requirement on the comagnetometer used to measure the magnetic field in the cell, which much be capable of, at worst, 16 fT resolution integrated over this period, in order to adequately correct the neutron measurement. Better resolution is desirable. As discussed in Section 1.5, in the case of ILL, the value for the comagnetometer was 200 fT, which was five times better than the neutron counting statistics. Here, we have set them equal.

In the ILL experiments, drifts and jumps in the magnetic field internal to the EDM cell of order 100 pT were observed. It was assumed that the comagnetometer corrected these drifts to the 200 fT level, i.e. by a factor of 500. Greater stability of the internal magnetic field would have reduced the reliance of the experiment on the comagnetometer. Conversely, it would have allowed the comagnetometer to be used to provide more stringent limits on more devious systematic effects, such as the effect of possible circulating leakage currents that could create a false EDM signal. Only the comagnetometer would be able to sense such an effect independently from the neutrons [22].

Magnetic surveys were conducted at TRIUMF in the area where the experiment will eventually be located [42]. The ambient field is $\sim$ 300 μT, dominated by the fringe field of the cyclotron. However, this dominant field can easily be suppressed with bucking coils, if it is stable. The key measurement is one of fluctuations of the ambient field over time. During quiet times at night, and restricting e.g. crane operation in the area, typical drifts in the magnetic field of $\sim$ 100 nT per hour were observed. Five orders of magnitude suppression of these drifts would therefore be required to reach the 1 pT goal set above. Or seven orders of magnitude would be required to reach 10 fT, stabilizing for example, to the required worst sensitivity of the comagnetometer per cycle.

Passive and active magnetic shielding will be used in the TRIUMF experiment to suppress the sensitivity of the experiment to variations in the ambient magnetic field. Calculations of a prototype passive magnetic shield have been conducted [24]. The prototype design consists of four concentric cylindrical shields. Endcaps with holes permit access. According to the simulation, a shielding factor of 10^6 should be achievable for an applied field of 50 μT in the axial direction [24]. The prototype design is approximately a half-scale prototype compared to the size required for the eventual experiment. The thickness of each shield would also be doubled in the eventual experiment,

so that the shielding factor would be the same.

Active magnetic shielding will be used external to the passive shield to suppress fluctuations. The general concepts of active magnetic shielding will be discussed in the next section. We have set a goal of $\sim$ two orders of magnitude suppression to be provided by the active magnetic shielding.

Overall, it is expected that the 100 nT fluctuations in the field at TRIUMF will be reduced to $\sim$ 1 nT fluctuations by the active shielding. This will be further suppressed by $\sim$ six orders of magnitude by the passive shielding to 1 fT. At this level, the field stability will be better than what is measurable by the neutrons, and might be better than what is measurable by the comagnetometer. Other magnetometers, such as super conducting quantum interference device (SQUID) magnetometers and alkali vapour atomic magnetometers, are being considered to aid in the characterization of the stability of the internal magnetic field.

1.7 Review of other feedback systems

Table 1.1 provides a summary of the active feedback systems reviewed. Many terms are used in the literature to describe the process of measuring and adjusting the magnetic field within a specific region. These include: active compensation, active shielding, dynamic shielding, magnetic field cancellation, magnetic field stabilization, or hybrid techniques (when accompanied by passive shielding) [4]. Regardless of name, the goal always remains the same: providing a stable magnetic field to a specified resolution in the presence of external perturbing fields. Of the active magnetic feedback systems reviewed from the literature, only one was specifically designed for a neutron EDM experiment [44], while the rest were designed for use in other experiments [6, 9, 18, 23, 29, 38], or specifically to provide suitable environments for biomagnetic measurements [16, 20, 21, 30, 33, 39]. In many cases the goal is to prevent soaring costs associated with large, multi-layered high permeability metal shields [16, 18]. In the case of the nEDM experiment at TRIUMF, active shielding is required mainly to achieve the desired magnetic field sensitivity of 1 fT, and to provide stabilization for low frequency disturbances. The lack of active shielding in most nEDM experiments suggests that the concept is still in its infancy, and that valuable ideas can be drawn from systems designed to

provide shielding for other purposes. This will help enhance our understanding of active shielding techniques in order to design a system to meet the resolution requirement of the experiment.

In terms of active shielding, each of the systems has a similar layout. A magnetic sensor is placed in or around the site of the desired low-field region. The sensor provides a magnetic field measurement to a controlling system. The controlling system adjusts the magnetic field by changing currents in a coil array. The field is then remeasured, producing a feedback loop.

The magnetic sensor can be as simple as a wire-wound coil [20], or more complicated like a flux-gate magnetometer [44] or a low-, or high-temperature superconducting quantum interference device (SQUID) [33,39]. In some cases numerous sensors are used to enhance the system performance [18], or provide the ability to actively shield regions where sensor placement is not possible [6,20]. In the case of multiple sensors, the signals are typically averaged over each axis and the combined voltage is fed to the controller to relay current to a pair of coils connected in series [18]. In some cases, each field sensor controls an independent coil, providing the ability to actively shield both uniform fields and gradients [6].

An interesting property of this type of system is that not all gradients require independent shielding. This can be seen, for example, from one of Maxwell's equations, $\vec{\nabla} \cdot \vec{B} = 0$, which states that

$$\frac{\partial B_x}{\partial x} + \frac{\partial B_y}{\partial y} + \frac{\partial B_z}{\partial z} = 0. \tag{1.15}$$

Therefore, if any two axes are actively zeroed from field gradients, the field gradients in the third axis must also be zero, and attempting to actively set the gradients to zero in all three directions will fail [9]. Similar conditions exist from $\vec{\nabla} \times \vec{B} = 0$ for transverse gradient terms.

The control system used to adjust the magnetic field typically calculates the error between the measured field and the desired set point. An algorithm known as PID control (described in further detail in Section 2.2) or some variation of the algorithm, calculates a response to the error, and sends an adjustment to a power supply controlling the current in the feedback coil system.

Typically, a strong interference component exists at the ac power line frequency (50- or 60-Hz) and its harmonics, which can burden the controller. To deal with this, some systems implement

specific detectors at these frequencies and add the amplified outputs to the compensation calculation [16, 21]. For the active shielding system developed in this work, a coil driven by the ac power line is used to reduce the 60-Hz interference.

The most commonly used coil system for providing uniform field adjustments is a Helmholtz-type configuration; however, some systems have had better success using the Alldred and Scoolar four-coil design, which provides better homogeneity [17]. When using the Alldred and Scoolar design for uniform fields, another set of coils (typically a Maxwell pair) is used for gradient field compensation [16, 39].

One method of designing the coils is to arrange them such that each one corrects a single component of the harmonic field expansion in a functional basis represented by eigenfunctions of the Laplace operator [7]. The performance of this method was not established.

The active shielding achieved by each of the reviewed systems varies greatly, but one commonality is that shielding factors are always larger for lower frequency disturbances. Common values of active shielding are on the order of 30-50 dB (∼30-300 times reduction in amplitude) for low-frequencies and 20 dB (×10 reduction) for frequencies approaching 500 Hz [33]. In the system intended for an nEDM experiment, measured shielding factors ranged from 10 times reduction at 50 Hz to 10^4 times reduction at 1 mHz [44]. A successful active shielding system, called a desktop shielding system due to its compact size [23], achieved a shielding factor of 70 dB (3162 times reduction) at frequencies below 1 Hz, and 42 dB (125.8 times reduction) up to 100 Hz.

Ref.	Field Sensor	Compensation Coil Type	Shielding Factor Obtained
[6]	2 magnetoresistive sensors	homogeneous 4 coil system over 1 axis, 2-coil system for gradients	30 dB $<$ 450 Hz for uniform fields, 20 dB $<$ 620 Hz for field gradients
[9]	5 single axis fluxgate magnetometers	Helmholtz, w/ indep. coils for 2 axes and series wiring for 3rd axis	28 dB reduction at 50 Hz
[16]	Active magnetoresistive sensor (AMR)	Alldred and Scoolar	15.5 dB at 100 Hz (gradient and homogenous field combination)
[18]	Unknown, 2 symmetrically placed sensors per axis	Square coil pairs, one per axis	25 dB from 1 to 10 Hz, 20 dB under 30 Hz,
[20]	Fluxgate magnetometer and normal wire-wound coil	5-turn coil	20 dB below 10 Hz, more than 20 dB for peak noises
[21]	60-turn wire-wound coil	5-turn ring coils, 5-turn Helmholtz coil pair	10 dB at 100 Hz 20 dB from 1-10 Hz
[23]	Orthogonal fluxgate magnetometer	10-turn Helmholtz-like coil pair	70 dB reduction at 1 Hz 42 db $\leq$ 100 Hz
[29]	Fluxgate magnetometer	3 coils over 1 axis	34.8 dB at 2 Hz, 26 dB at 10 Hz, 14 dB at 50 Hz
[30]	3 othogonal SQUID magnetometers	3-axis Helmholtz-like coil set	23 dB at 50 mHz
[33]	low-Tc SQUID magnetometer	3-axis Helmholtz coil set	Over 40 dB below 0.1 Hz, $<$20 dB at 1 Hz
[38]	Fluxgate magnetometer	Helmholtz pair	60 dB $<$ 5 Hz
[39]	Air-cored induction-coil magnetometer	Alldred and Scoolar	43.5 dB from 1 to 10 Hz, 26 dB at 100 Hz
[44]	Multiple Three-axis fluxgate magnetometers	homogeneous 4 rectangular coil system over 1 axis	100 dB at 1 mHz, 20 dB at 50 Hz

Table 1.1: A summary of the magnetic field sensors and compensation coils used in the active shielding systems reviewed, as well as the shielding factors obtained for each system.

1.8 Thesis overview

This thesis focuses on the development and testing of a prototype active magnetic shielding system for the TRIUMF nEDM experiment. The system is based on the measurement of magnetic fields from a 3-axis fluxgate sensor, centered in a 3-axis Helmholtz-like coil set. The measurement is sent

to an analog-to-digital converter (ADC), and a software based controller operating on a computer uses the ADC output to calculate the error of the measurement relative to a desired magnetic field set point (zero in this case). The software uses a proportional-integral-derivative (PID) algorithm to calculate the current requirement in the coil set to drive the field to zero. The PID output is transmitted to a digital-to-analog converter (DAC) as a voltage, and a proportional voltage amplifier powered by a dc supply uses the DAC output as a controlling voltage to drive the calculated current into the coil set. This represents one cycle of the continuous control loop used to reduce the magnitude of near-dc magnetic fields. This thesis will present the details of the prototype active shielding system. Tests of the shielding system performance will be analyzed to determine limitations, and suggestions will be provided to guide future development.

Chapter 2

Process control

As mentioned previously, the nEDM experiment requires a null background magnetic field which must be monitored and controlled to extreme precision. This is just one of the many scientific applications that require an automated way to stabilize a system parameter in the presence of disturbances. The parameter being examined could be anything from the power levels in lasers, to flow rates of fluid systems, or in the case of this project, magnetic fields in the nEDM experiment. The action of continually measuring a system variable, and performing adjustments to that variable based on the measurement is called process control. Process control is a discipline of statistics and engineering dealing with a process variable, comparison of the variable to a set point, and manipulation of the process to bring the variable to the set point. The goal is to keep the process variable as close as possible to the set point, especially during disturbances to the system resulting in uncontrollable process variable changes.

As an example, consider the magnetic field in the nEDM experiment. The magnetic field in the experimental region is a process variable, and the set point is zero. The measurement of the magnetic field changes when extraneous events cause magnetic field disturbances in the experimental region. Manipulation of the magnetic field is achieved by driving current into a coil surrounding the experiment, bringing the field to the set point. Maintaining the set point as the field measurement changes requires current adjustments in the compensation coil, and ideally a system is set in place to track the field changes and implement the current adjustments. In this example, the magnetic field

in the experimental region is known as the measured or controlled variable and the field produced by the current adjustments in the compensation coil is known as the manipulated variable. The measured variable and manipulated variable pair, along with a control algorithm linking the two, is referred to as a control loop.

2.1 The control loop

There are four main elements to the process control loop:

1. Measurement of a process variable: A sensor, or transmitter, measures some variable in the process such as temperature, volume, or pressure, and converts the measurement into a signal which can be interpreted by the controller. For our control loop, the process variable is the total magnetic field in our specified control region, measured by a fluxgate sensor.

2. Control algorithm: A mathematical algorithm executed by the control system which calculates the output signal for transmission to the control element. The control algorithm is designed to respond to changes in the set point, which are typically user defined, as well as changes in the system loads, which are environmental perturbations. It is also important that the algorithm prevent the loop from becoming unstable and exhibiting oscillatory behavior. For our purpose of actively shielding magnetic fields, we use a proportional-integral-derivative (PID) control algorithm, which will be explained later.

3. Control element: A device that receives the output signal from the control algorithm and executes its command, changing a manipulated variable, and manipulating the process. In our active shielding apparatus, the control element is the current driven into a set of coils, producing a corresponding magnetic field which is the manipulated variable.

4. The Process: A response to changes in the manipulated variable and external perturbations, resulting in a change of the measured variable. The response of the process to changes is a significant factor in choosing the appropriate parameters for the control algorithm. The process in our control loop is the combination of adjusting the current in a coil set to produce

a compensating magnetic field, and the environmental magnetic field which we have no control over. Together, these two field contributions form the total magnetic field, which is the measured variable in our system.

The connection between the control loop elements is shown in Figure 2.1.

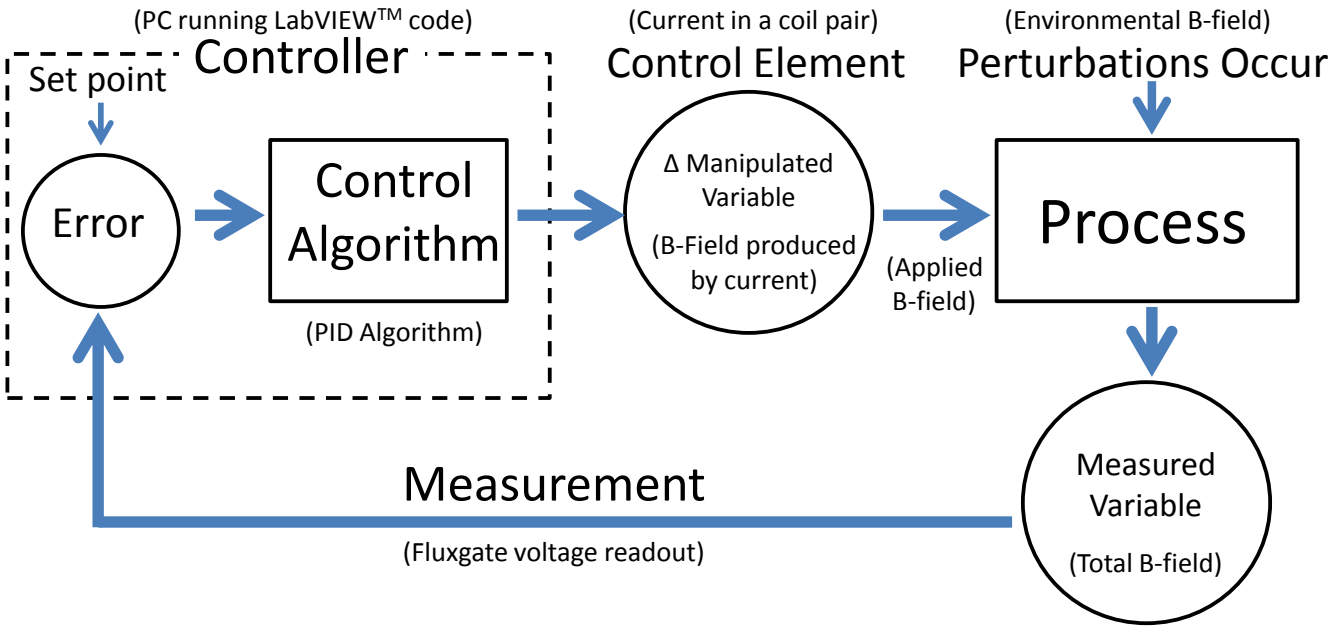

Figure 2.1: The connection between elements of a typical control loop. The text in parentheses in the figure describe the related component of our active feedback system. Beginning with a process which is subject to perturbations (environmental magnetic field), a measurement of the process variable (total magnetic field) is performed and transmitted to the controller (PC running LabVIEW^{TM} code). The controller determines difference between the measurement and the set point (zero for active magnetic shielding), and the resulting error is sent to the control algorithm (PID). The controller transmits the output of the control algorithm to the control element (current in a coil pair), which changes the manipulated variable (magnetic field produced by the current in the coil pair), counteracting perturbations to the process and bringing it to the set point. This completes the loop, which continues to cycle through its steps to maintain the measured variable at the set point.

A simple example of a control loop is maintaining the temperature in a house. When the temperature (measured variable) drops below the thermostat (controller) temperature setting (set point), the thermostat engages the furnace (control element) which adds heat (manipulated variable) to the house. As long as the temperature is below the thermostat setting the furnace remains on. Once the temperature reaches or exceeds the thermostat setting, the furnace is turned off. The control algorithm in this example is an on/off switch, which is sufficient for most households. Substituting

a mathematical algorithm for the on/off switch can provide better control, and the most common is the PID algorithm, described in the following section.

2.2 The PID algorithm basics

An overview of the main ideas of the PID algorithm is given here. A more in depth discussion of PID control can be found in the References [1, 43].

The PID algorithm, which stands for Proportional-Integral-Derivative, is the most commonly used algorithm in industrial process control and is used in the active magnetic shielding system discussed in this thesis. The PID control algorithm uses no a priori knowledge of how the system behaves or what the correct output is that will bring the process to the set point. By means of feedback (looped process measurement), the PID algorithm changes the output in a direction that should move the process toward the set point until it is reached.

2.2.1 Action

A PID system has two types of basic action with respect to the control direction of the manipulated variable. The first is direct action, which produces an increase in the manipulated variable whenever the process value is greater than the set value. An example of this is a cooling application where the temperature is greater than the thermostat setting. This requires an increase in the cooling action. Reverse action is the opposite, which produces a decrease in the manipulated variable whenever the process value is larger than the set value. In the cooling application example, when temperature passes below the thermostat setting, the cooling action is reduced.

2.2.2 Error

The error (e) of the control loop is defined as the difference between the set point (SP) and the process variable measurement (PV):

$$e = SP - PV. \tag{2.1}$$

The error provides the controller with a measure of the required adjustment to the system. The error is typically used in calculations involving each of the control algorithm parameters to determine the output of the algorithm.

2.2.3 PID parameters

As mentioned previously, there are three parameters in the PID algorithm, Proportional (P), Integral (I), and Derivative (D). The details of each parameter are briefly discussed below. For further details, refer to the cited references at the beginning of Section 2.2.

Proportional control

Proportional (P) control adjusts the manipulated variable (MV) in proportion to the error (e). Using P control action, the MV is calculated by multiplying a proportional gain factor, denoted by K_P, with the error value

$$MV = K_P \times e\,. \tag{2.2}$$

Proportional control works in the following manner. When K_P is large, the system produces a large change in the output for a given change in the error. A large value of K_P can cause the system to oscillate about the set value before settling. If K_P is set too high, the system can become unstable and oscillate uncontrollably and indefinitely. Conversely, if K_P is set too low the system will respond slowly, approaching the set value and eventually settling. The P-control behavior for large and small values of K_P is shown in Figure 2.2.

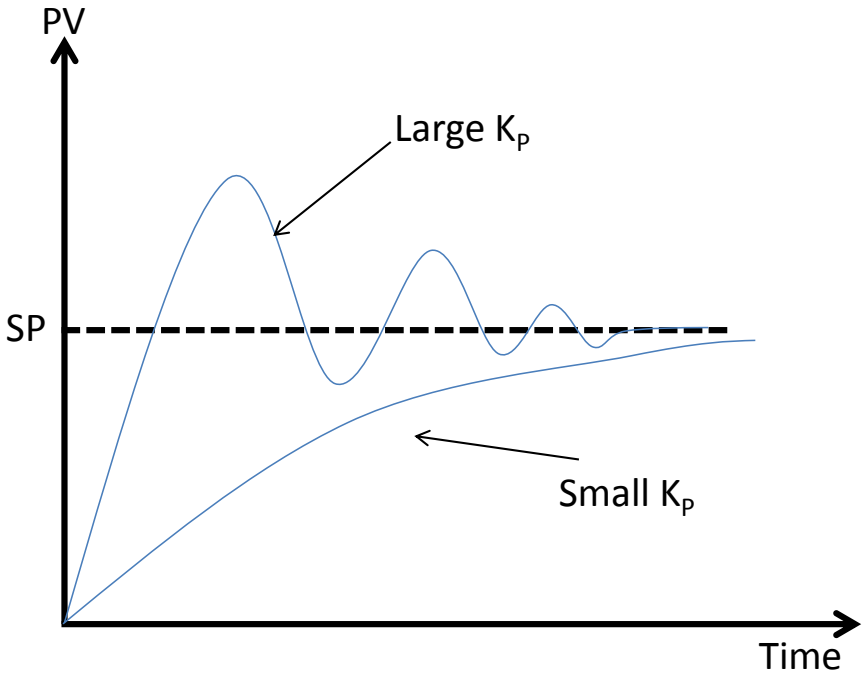

Figure 2.2: Proportional control behavior for two different values of K_P. The large K_P causes oscillations about the set point that eventually settle. The small K_P slowly approaches the set point and eventually settles.

P control can be thought of as an adjustment based on the present state of the system.

Integral (I) control

Integral control adjusts the manipulated variable in proportion to the time-integral of the error. If any error exists, the integral control modulates the manipulated variable to eliminate the error. Integral control is calculated in the following way:

$$MV = K_I \times \int_0^t e\, dt, \tag{2.3}$$

where K_I is the integral gain, and integration time is the period of the process variable measurement. Large values of K_I result in the system output changing rapidly, typically causing oscillations about the set point that eventually settle. If K_I is too large the system will oscillate uncontrollably. If K_I is too small, the manipulated variable changes slowly and the system will take more time to reach the set value. The I control behavior is shown in Figure 2.3 for three values of K_I.

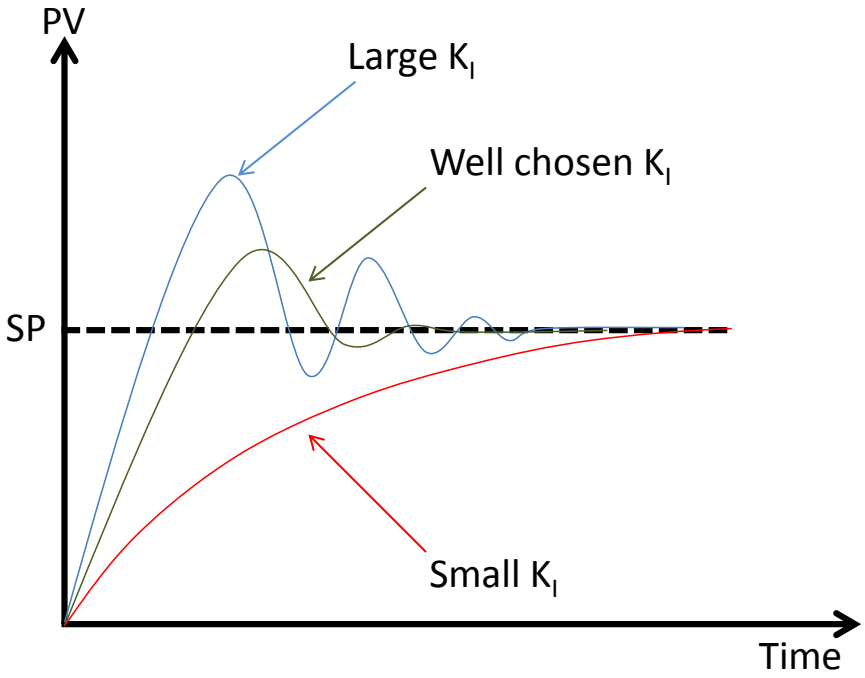

Figure 2.3: Integral control behavior with three different values of K_I. The large K_I sets the system into oscillations eventually reaching the set point. The small K_I does not cause oscillations, however it takes longer to reach the set point than with the large K_I. The well chosen K_I causes a brief overshoot, but brings the process to the set point the fastest, which is the desired result.

The I-control output is the sum of the most recent, and all previous I-calculations up to a set number. This number is known as the integral reset, and it is set based on the properties of the system such as how often a change in the external perturbation occurs. I-control can be thought of as an adjustment based on the past error of the system.

I-control is never used by itself, and is always paired with proportional control (PI-controller). These can also be combined with derivative control.

Derivative control

Derivative control adjusts the manipulated variable in proportion to the rate of change of the error. This serves as a quick corrective action when a sudden change in the process occurs. The manipulated value from the derivative control is typically calculated as follows:

$$MV = K_D \times \frac{de}{dt}, \tag{2.4}$$

where K_D is the derivative gain and dt is the period of the process variable measurement.

Derivative control attempts to predict system behavior and improve settling time and stability of the system. Derivative control is not suited for rapidly oscillating processes and is rarely used for processes which respond quickly. Derivative control is very sensitive to measurement noise, and can produce erratic changes to the manipulated variable which can degrade control performance. Sudden changes in the measured error can cause large changes in the control action, sometimes called derivative kick.

The theory of derivative control suggests that increasing K_D will improve stability in the system, however experimentally, it is found that the K_D term can produce adverse effects. Tuning K_D can often times be frustrating and produce little to no results, leading to many practitioners turning off or abandoning the derivative term altogether [1].

Combining P, I, and D into one algorithm

The P, I, and D control elements are combined into one algorithm by summing the results of each calculation as follows:

$$\text{PID Output} = K_P \times e + K_I \int_0^t e\,dt + K_D \frac{de}{dt}, \tag{2.5}$$

where as mentioned before, K_P, K_I, and K_D are the proportional, integral, and derivative parameters respectively. e is the error calculated by subtracting the process value from the set point, and dt is the period of the process variable measurement.

The control algorithm used for active shielding in this thesis contains the entire PID calculation. Through adjusting the three parameters, it was found that the derivative term produced erratic behavior in the controller output and did not provide any benefit to the active shielding tests described later. For this reason, K_D was set to zero for all tests, but remains available for future consideration.

2.2.4 PID tuning

The parameters of the PID control algorithm must be adjusted for the specific process loop. This is known as tuning. Without proper tuning, the algorithm will not perform optimally, and may produce unwanted effects. PID tuning is based on the dynamics of the process response, and varies with different types of perturbations. A basic tuning strategy is to make adjustments to each of the PID parameters until the process variable measurement is a close as possible to the set point. More advanced tuning methods are outside the scope of this project, but will likely be employed in future iterations. For more information, please see the references cited at the beginning of Section 2.2.

Chapter 3

Active feedback system for magnetic field control

The 3 main elements of the prototype active shielding system used in this thesis are shown in Figure 3.1. These are (i) measurement of a magnetic field, (ii) error and current calculation, and (iii) control of magnetic field. The individual components of the system are discussed in greater detail in the following sections.

For the purpose of this thesis we will attempt to control the x-, y-, and z-components of the magnetic field at the center of a 3-axis Helmholtz-like coil set (hence force referred to as the "coil cube"). Measurements of the magnetic field at the centre of the coil cube are performed using a single 3-axis fluxgate magnetometer. This information is input to a PID algorithm, written using National Instruments (NI) LabVIEW^{TM}, which in turn controls the current driven in the coil cube by a dc amplifier. In the following chapter the performance of each device will be analyzed to determine if limitations exist that may affect system performance.

As mentioned in Section 1.8, this system is a prototype of an active magnetic shielding system for the nEDM experiment at TRIUMF. This is a first iteration of what will undoubtedly become a significantly more complex system, and its purpose is to provide initial research and development for the final shielding system. The work presented in this thesis focused on determining and characterizing the fundamental constraints that affect shielding efficacy. As such, it provides information

that will help tailor the next version of the active shielding system.

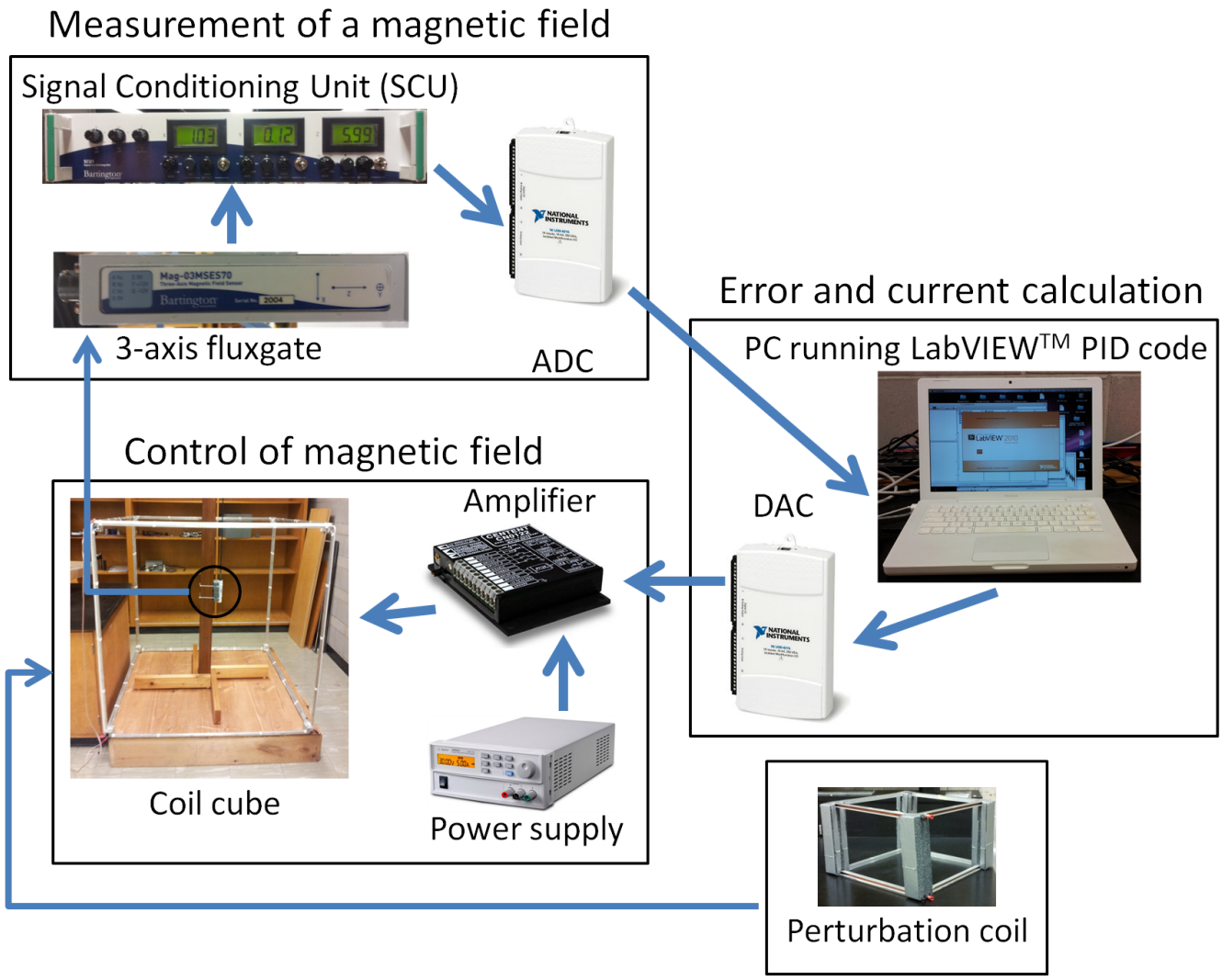

Figure 3.1: The components of the active shielding system prototype grouped by control loop element. The control loop begins with a measurement of the total magnetic field (process variable) at the center of the coil cube. The output from the fluxgate, typically low-pass filtered by the SCU, is digitized by the ADC and passed to the PC for error and current calculations via a PID algorithm (controller). The controller determines what should be the updated coil current, which is passed as an analog voltage signal to the current amplifier via the DAC. The amplifier drives the coil cube by drawing the required current from the dc power supply. A final component needed for test purposes is an independent coil, used to provide magnetic field perturbations of known frequency and amplitude to region of interest. For the sake of clarity, the perturbation coil is not shown in its experimental location, centered about the fluxgate.

3.1 Active feedback system overview

The electronics chain of the active feedback system (shown in Figure 3.1) begins with a single 3-axis fluxgate magnetometer centered in a 3-axis Helmholtz-like coil set. After passing through the signal conditioning unit (SCU), capable of low- and high-pass filtering plus measurement gain (amplification), the analog signal is sent to an analog-to-digital converter (ADC). The digitized signal is then passed to a Macbook personal computer via a universal serial bus (USB) connection. The computer performs an error and current calculation and the output is sent back through the USB connection to a digital to analog conveter (DAC). The analog signal is fed to an amplifier which draws the calculated current from a power supply and drives it into the coil set, changing the field to the desired set point. A separate coil is used to apply magnetic field perturbations for active shielding tests. Each component of the system will be described separately in the following sections.

3.2 Fluxgates and signal conditioning unit

To perform magnetic field measurements for this work, the Bartington Mag-03MSES70 3-axis magnetic field sensor, shown in Figure 3.1, was used. It contains three single-axis sensors directed orthogonally to one another, all contained within a $32 \times 32 \times 152$ mm^3 sealed enclosure. Each sensor converts magnetic field into a bipolar analog voltage in linear proportion to the field magnitude along the sensor axis. This fluxgate model has a range of ± 70 μT, with a $\pm$ 5nT offset and a noise floor of 6-10 pTrms/$\sqrt{\text{Hz}}$ specified at 1 Hz. It should be noted that the offset and noise floor are well below noise levels of the background fields in the experimental region of interest. The manufacturers specifications for our fluxgate is shown in Table B.1 in Section B.1 of the appendix. The basic inner workings of a fluxgate sensor are described in Appendix A.

The 3-axis sensor is both powered and read by the Bartington Mag-03SCU signal conditioning unit (SCU), shown in Figure 3.1, which has a $\pm$10V full scale output. The SCU allows one to filter (low-, and high-pass) the output signals of each fluxgates, as well as adjust the gain and offset of the

of each channel independently. The low-pass filter (LPF) settings are 1, 10, 100, 1000 and 10000 Hz. The high-pass filter (HPF) settings are 0.01 Hz, 1 Hz, and off. For this work we are predominantly interested in dc and low-frequency fields, and as a result did not use the HPF and typically set the LPF to 1 KHz. The latter removed high-frequency noise while remaining well above the 400-Hz maximum sampling rate of our control loop, as discussed in Section 3.4 later. Also, because our interest lies in compensating fields of order the magnitude of Earth's field, the lowest gain was used, providing an output of 7 μT/V. As a point of reference, the typical background field components at the location of the fluxgate at the center of the coil cube are $B_x = 14$ μT, $B_y = 1.4$ μT, and $B_z = 41$ μT, where the x-direction lies roughly North-South, the y-direction is East-West, and the z-direction is along the vertical.

3.3 Analog to digital conversion

An analog to digital converter (ADC) is required to convert the analog signal from the SCU to a digital signal which can be interpreted by the computer. The ADC used for this project is a National Instruments (NI) USB-6215, a bus-powered isolated USB multifunction data aquisition (DAQ) module (shown in Figure 3.1). The USB connection makes it easy to integrate into a system running LabVIEW$^{\text{TM}}$, such as the active feedback system presented in this thesis. It has sixteen, 16-bit analog inputs capable of a combined total of 250 kilo-samples per second (250 kS/s) over a variable input voltage range.

The voltage range of the input can be adjusted from a maximum of $\pm$10 Volts to a minimum of $\pm$1 Volts, which changes the input precision. Since the output voltage of the sensor used for magnetic field measurements is $\pm$10 Volts, the maximum input range of the ADC was used to perform the signal conversion. The input precision can be calculated by dividing the 16 bits over the $\pm$10 Volt range as follows:

$$\text{Input precision} = \frac{20\,V}{2^{16}} = \frac{20\,V}{65536} = 0.000305\,V = 305\,\mu V. \tag{3.1}$$

However, the USB-621x device series are calibrated in such a way that a portion (typically about 5 %) of the voltage codes for a given voltage range will lie outside of that voltage range. This helps to improve absolute accuracy, but it increases the nominal resolution of input ranges by about 5 % over the calculation above. As a result, the actual input precision is 320 μV. Recalling from above that the sensitivity of the field measurement via the SCU is 7 μT/V, digitization at the 320 μV level corresponds to a resolution of 2.24 nT, which again is well above the noise floor of the fluxgate. Therefore, the resolution of the field measurement is ultimately limited by the ADC.

3.4 PID control

At the heart of the feedback system is a PID controller coded in LabVIEW^{TM}, as shown in Figure 3.2. LabVIEW^{TM} is not a conventional text-based coding environment, rather, coding is achieved by assembling a group of control elements, linked by "wires". LabVIEW^{TM} code is typically programmed with both a front and back end. The front end, which is a graphical user interface (GUI), can provide information about, and control over the inner working code in the form of charts, plots, gauges, numerical displays, and other graphical objects. The back end is a collection of connected control element icons. The icons represent signal queries from hardware, mathematical calculations, timers, loops, and any other conventional programming element. The connection between icons using wires represents data passing between the programming elements, and the order of the connections determines the sequence of operations.

The PID controller coded for this work was designed with a GUI front end, primarily used for adjusting the PID parameters and viewing the immediate results of active field compensation. The main structure of the code is a loop that takes the most recent value of the magnetic field from the ADC and performs a calculation based on the set point and the specified PID parameters. Since this is a software loop, the rate at which it operates is based on how fast the computer can execute each loop in combination with the communication time between the software and the DAQ. Presently, the software operates at a maximum rate of $\sim$ 400 Hz if no interruptions are present (the ramifications of this limit will be discussed further in Section 5.3). In order to reduce the operating

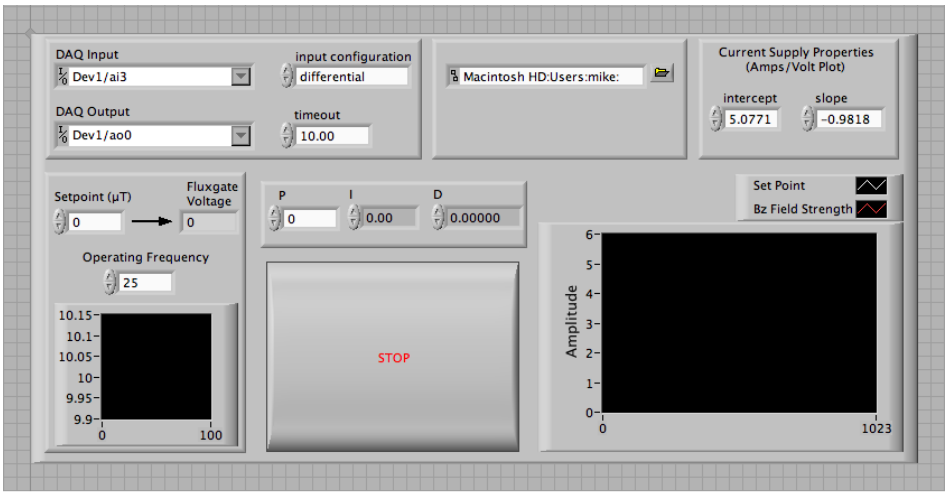

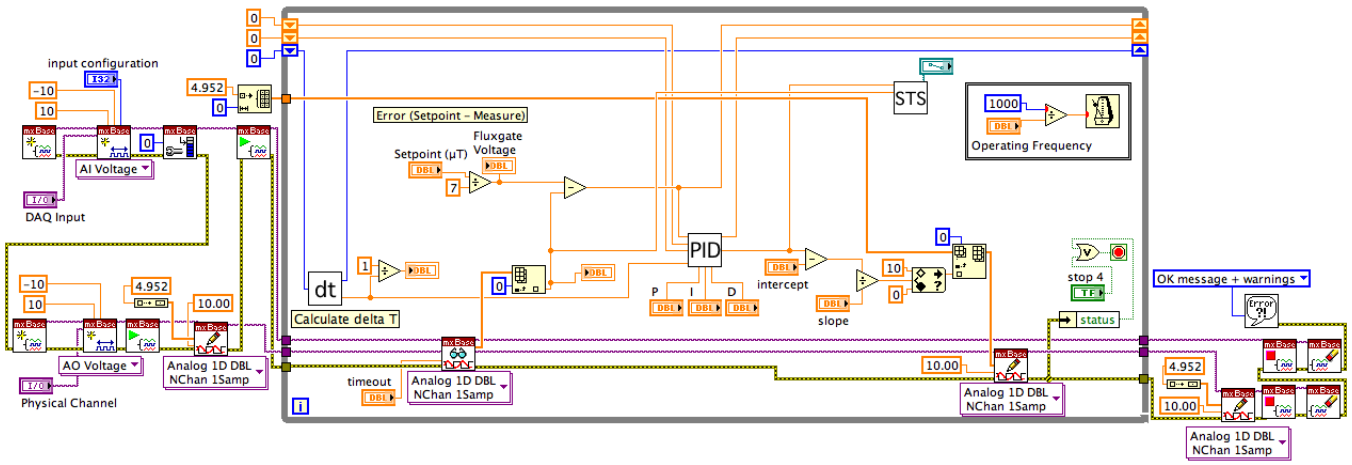

Figure 3.2: Top: Front end GUI of the LabVIEW™ coded PID controller used in this project. The interface provides control over the input and output channels of the NI USB-6215 DAQ, the name and location of the data file for logging results, the current amplifier calibration, and most important, the desired setpoint, PID parameters, and the sampling rate used for active shielding. The setpoint and magnetic field measurements are simultaneously displayed in a plot, located in the bottom right corner, which is updated at each field measurement. Bottom: Back end of the LabVIEW™ coded PID controller used in this project. A while loop, represented by the central rectangular structure, uses the voltage input from the ADC (configured outside and to the left of the structure) to perform an error and PID calculation using the front end GUI input parameters. The calculation is output to the DAC and the loop resets after a timer within the loop performs a waiting operation to set the loop frequency.

frequency, a timer is placed within the main control loop which serves to add a controllable amount of delay at the end of each loop. By adjusting the length of the delay in the loop, the operating rate of the control system can be set. The sampling rate of the magnetic field for active shielding is the same as the operating rate of the control loop, since the field is only sampled at the beginning

of each loop.

3.5 Digital to analog conversion

A digital to analog converter (DAC) is used to convert the digital signal from the LabVIEW^{TM} PID output to an analog signal that the amplifier can use. The same NI USB-6215 DAQ module used for the ADC task is also used here. The DAC portion of the module has two analog outputs (16-bit each, 250 kS/s combined) with a $\pm$10 V output range. As with the input, the resolution on the output is nominally 320 μV.

3.6 Power supply

We tested several power supplies to provide the 3-axis coil cube with the necessary current for active shielding. These included an HP 6624A dc power supply, an Agilent 6655A dc power supply, a Texio PR36-3A dc power supply, and finally an Agilent U8002A. The first two power supplies are programmable via either GPIB control or analog voltage input, and were connected to the LabVIEW^{TM} output via separate USB and the DAC, respectively. However, none of these alone could provide the current resolution required to achieve the desired result, nor could they provide the bipolar current required to actively shield a variety of magnetic fields. The final solution was to use a Centent CN0122 bi-directional amplifier, as described next, powered by the Agilent U8002A power supply.

The Agilent U8002A, provides up to 5 A at 30 V for a maximum power output of 150 W. This supply provides a voltage resolution of 10 mV and a current resolution of 10 mA. The full specifications are listed in Figure B.2 in Section B.2 of the Appendix.

3.7 Amplifier

The CN0122 is an H-Bridge servo amplifier dc motor control designed for bi-directional operation of permanent magnet motors. The amplifier can operate in either a speed control or torque control

mode which provide different functionality. In torque control mode the amplifier outputs a current proportional to an input voltage, and as such can be used here to convert the analog output from the DAC to a current used to drive the coil cube. The CN0122 can supply up to ± 5A at 32 V, which is more than sufficient for our present purpose. Important performance tests of the CN0122, especially the resolution of the current output are described in the following chapter. The full specifications for the CN0122 are listed in Figure B.3 in Section B.3 of the Appendix.

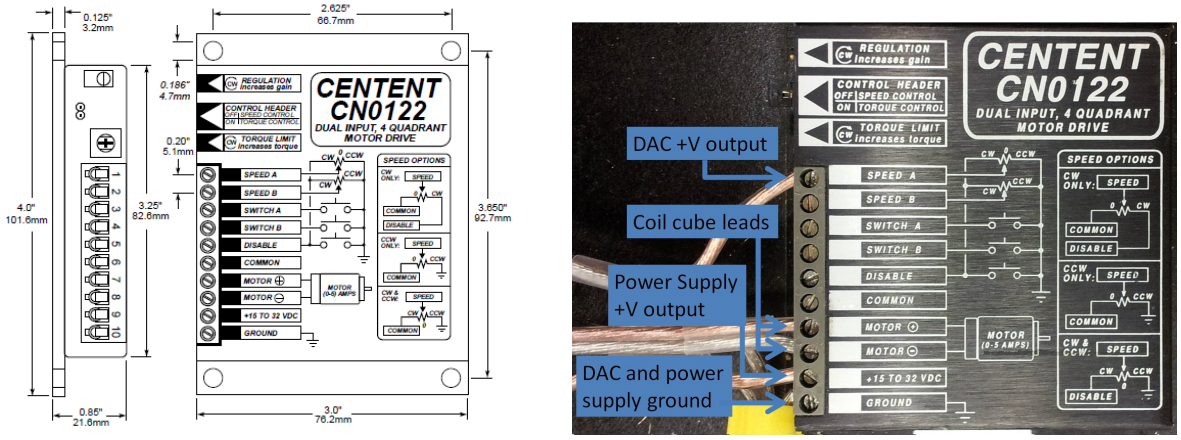

Figure 3.3: Centent CN0122 dual input motor drive. Left: Drawing of the Centent CN0122. Right: Picture of the Centent CN0122 used in this work. The labels indicate how the device was connected in the present apparatus.

3.8 Coil cube

To adjust the magnetic field at the location of the fluxgate sensor, wire-wound coils surrounding the sensor are driven with currents to produce magnetic fields which are used to counteract perturbing fields. A 3-axis Helmholtz-like coil set(shown in Figure 3.1) was used due to the fact that it provides a large central uniform region of magnetic field, and a set was readily available for use at the University of Winnipeg. The three coil pairs form a cube with sides of 45 inches in length. The self resonant frequency of each coil pair is of order 300 kHz, three orders of magnitude greater than any frequency of concern for the work presented here. The important basic physical parameters of the coil cube are given in Table 3.1, and all relevant tests of the coil cube performance are presented in the following chapter.

Axis	R (Ω)	L (mH)	χ (μT/A)
X	20	23	40
Y	13	19	34
Z	16	23	40

Table 3.1: Basic physical parameters of the coil cube. Resistance (R), inductance (L) and coil constant (χ) for each of the x-, y-, and $z-$coil pairs.

3.9 Perturbation coil

In order to test the active shielding ability of the feedback system, a magnetic perturbation is applied to the compensation region and the system is engaged. Comparison of the perturbation strength before compensation with the residual field during compensation provides a measure of the shielding factor.

The perturbation field is applied using a Helmholtz coil pair assembled from two 13.5" x 13.5" aluminum u-channel framed coils, as shown in Figure 3.4. The coil spacing was determined by taking 0.5445 times the length of each side, which is the optimal spacing for a Helmholtz pair assembled with square coils [14].

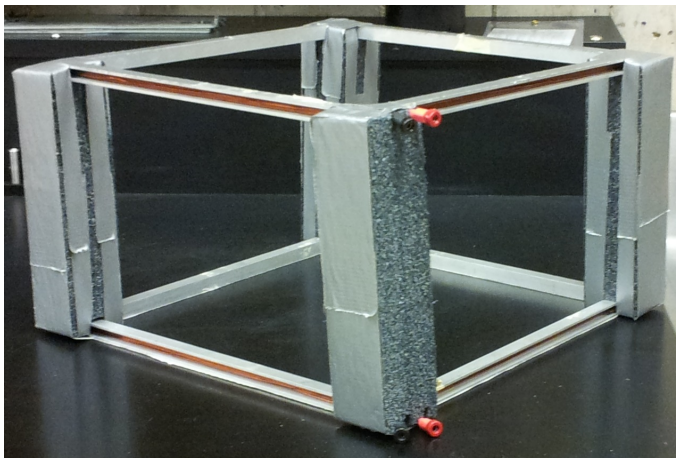

Figure 3.4: Perturbation coil assembled by combining two aluminum u-channel framed coils in a Helmholtz configuration.

The perturbation coil pair was centered about the fluxgate within the coil cube. This ensures a uniform perturbation field over the volume of the z-axis sensor. To drive the perturbation, the

coil was connected to a separate Centent CN0122 amplifier powered by an Agilent 6655A dc power supply. The controlling input voltage for the amplifier was a sinusoid output from an Agilent 33210A function generator.

Chapter 4

Resolution and performance of the active shielding system components

Characterizing the system requires knowledge of its individual components. Since each device in the electronics chain could potentially introduce a limitation into the feedback system, it is important to understand these limitations individually to better understand the system as a whole. In this section the resolution of each component of the system will be discussed in order of their appearance in the control loop. Following this, tests of individual components and combinations of components will be shown.

4.1 Fluxgate frequency response

The frequency response for the Bartington Mag-03MSES70 sensor was tested by applying external magnetic ac fields using a small wire coil. The fields were applied with constant amplitude and varying frequency up to 5 KHz while the voltage output from the fluxgate was monitored. Figure 4.1 shows the results of the test for the z-axis field sensor. The frequency response is more or less flat up to 1 KHz. Since the typical low-pass filter setting on the SCU is 1 KHz during active shielding experiments, the frequency response test confirms that the total magnetic field up to the low-pass filter frequency setting is measured.

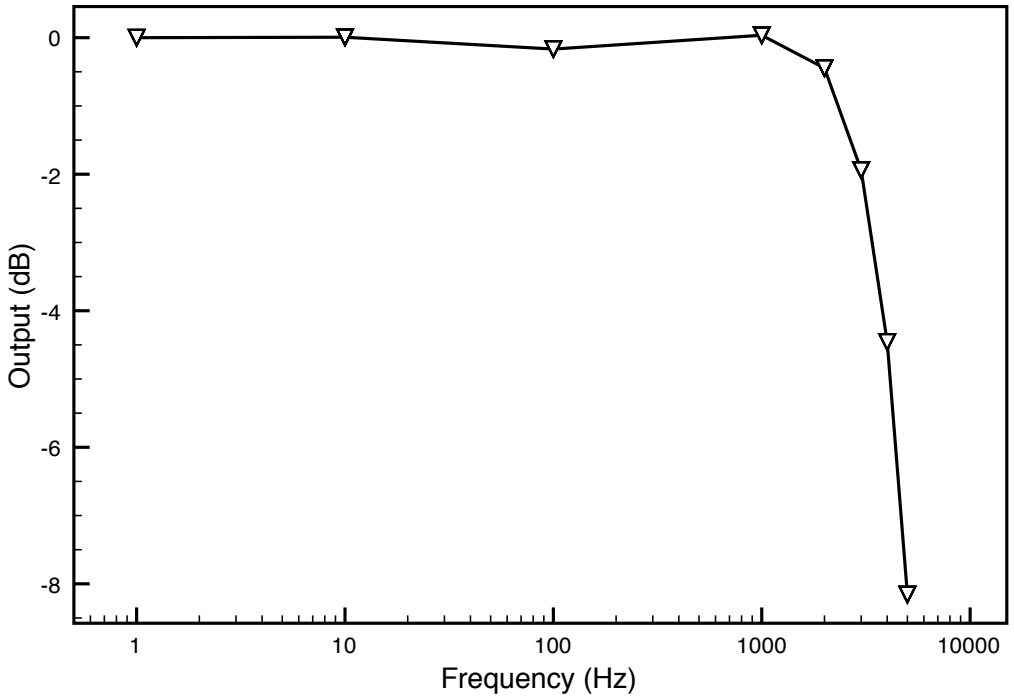

Figure 4.1: Frequency response of the z-axis field sensor in the Bartington Mag-03MSES70 fluxgate. The output measurement remains more or less flat up to 1000 Hz, at which point it begins to decrease.

4.2 Centent CN0122 amplifier tests

To test the output of the Centent CN0122 amplifier, it was powered by a Texio PR36-3A regulated dc power supply, and its output was connected to the z-coil pair. The input voltage was varied and the voltage and current output were measured using digital multi-meters (DMMs). A schematic of the experimental setup is shown in Figure 4.2, and the results of the test are shown in Table 4.1.

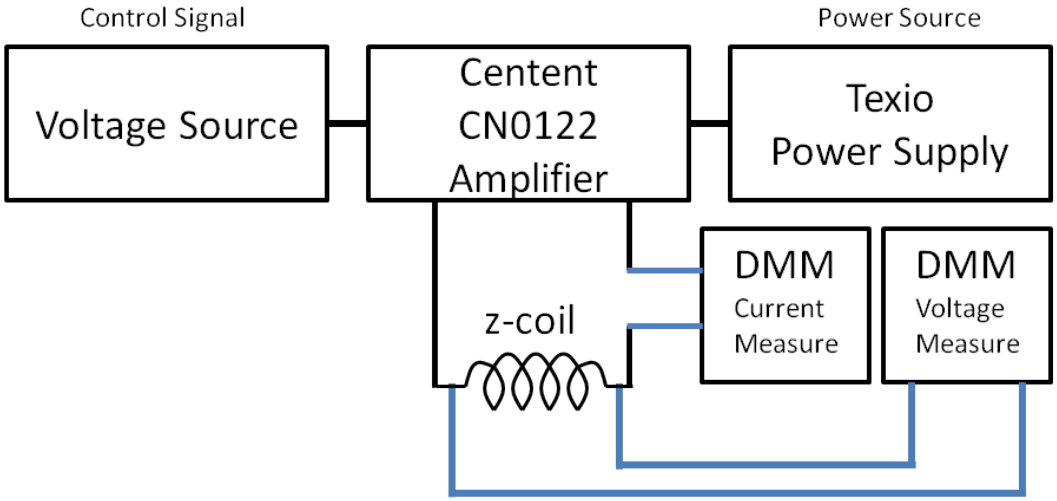

Figure 4.2: Schematic of the experimental setup used to test the output of the Centent CN0122 amplifier.

V_{Input} (V)	V_{Output} (V)	I_{Output} (A)
7.074	-29.923	-1.865
5.162	0.005	0.003
3.283	29.639	1.857

Table 4.1: Centent CN0122 torque control mode voltage and current output.

Our main interest lies in the current output of the amplifier relative to the input voltage. This was calculated from the aforementioned data and is

$$I_{output} = -0.9818 \times V_{input} + 5.0771. \tag{4.1}$$

The amplifier outputs a change of nearly 1 A of current per input volt change, with an output polarity crossing at ≈5 V.

One issue with the CN0122 is that when switching polarity on the output it introduces a glitch around the zero-crossing point of the amplifier. This was tested by using a step function for the input of the amplifier and monitoring the current output using an oscilloscope. Figure 4.3 illustrates that the zero-crossing glitch is real, and by offsetting the input voltage step to the amplifier either above or below the zero-crossing, the glitch is eliminated.

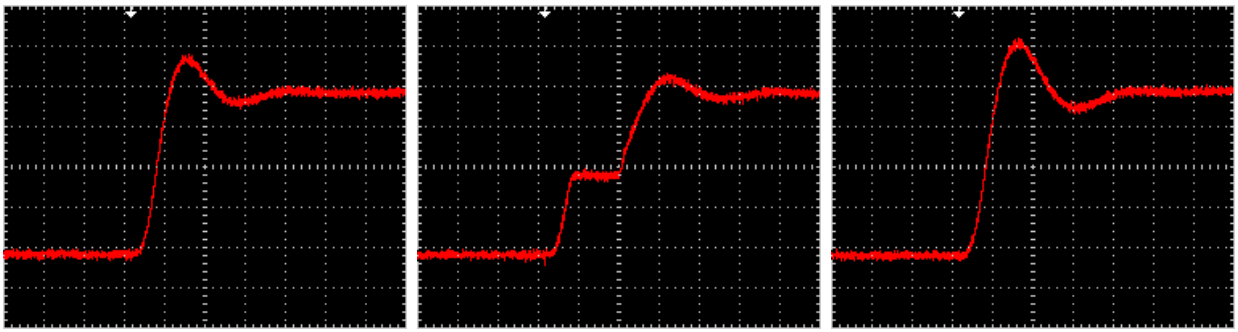

(a) **(b)** **(c)**

Figure 4.3: Current output of Centent CN0122 amplifier with a step function as the voltage input. Oscilloscope screen captures are shown for a step function (a) offset above, (b) centered on, and (c) offset below the zero-crossing. The vertical scale is 500 mV per division and the horizontal scale is 10 μs per division. Figure (b), where step function is centered on the amplifier zero-crossing, shows that as the amplifier output passes through its zero-crossing the change in current ceases for $\sim$ 10 μs. This feature is not seen in Figures (a) or (b) where the step function is offset above and below the zero-crossing, respectively.

This is especially apparent when the amplifier is outputting current to a high reactive load, $X_L = \omega L$. This indicates that the reactive component of the total impedance is responsible for the output glitch. To test this, the amplifier was set up to drive the z-axis coil pair in series with a 1 Ω power resistor, using a function generator outputting a sinusoid as the amplifiers input voltage. The frequency of the function generator output was set to several values and the current at the 1 Ω resistor was monitored for each frequency. The results are shown in Figure 4.4.

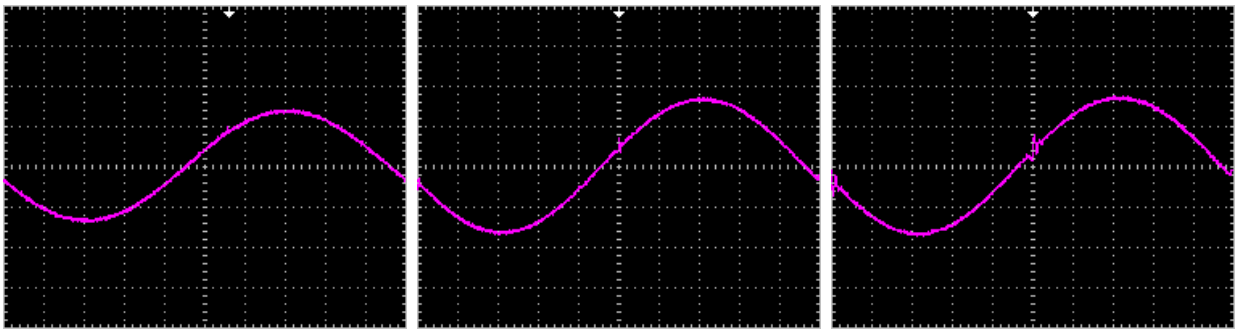

(a) 1-Hz sinusoid **(b)** 4-Hz sinusoid **(c)** 10-Hz sinusoid

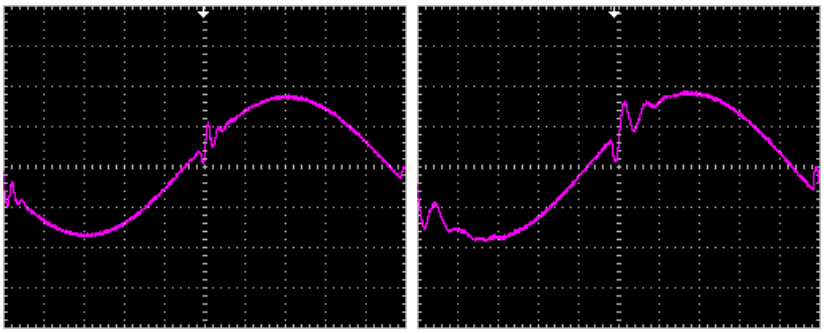

(d) 20-Hz sinusoid **(e)** 40-Hz sinusoid

Figure 4.4: Current output of the Centent CN0122 amplifier driving the z-coil pair with a function generator sinusoid as its input voltage. Oscilloscope screen captures are shown for several frequencies of the input voltage sinusoid. In each image the vertical scale is 5 V per division, and the horizontal scales are 100 ms, 25 ms, 10 ms, 5 ms, and 2.5 ms in order from (a) to (e). Figure (a) shows no sign of current output issues for a 1-Hz sinusoid, however, a small current glitch is present for the 4-Hz sinusoid voltage input, and as the frequency of the voltage input increases, the current glitch becomes more pronounced.

Figure 4.4 shows that as the frequency of the sinusoid increases, so too does the magnitude of the current glitch near the zero-crossing point. To test if this issue stems from an increase in the purely resistive load, the z-coil pair was replaced with a variable resistor. To determine the appropriate resistances to load the amplifier output with, the total impedance of the previous setup was determined for each of the driving frequencies. The z-coil pair has a previously measured inductance of 23 mH, making the calculation possible using the formula for impedance of an inductive load:

$$|Z| = \sqrt{R^2 + \omega^2 L^2} \ . \tag{4.2}$$

Table 4.2 gives the calculated values for the impedance of the coil for each of the tested frequencies.

$f(Hz)$	ωL	$\lvert Z \rvert$
1	0.145	16.00
4	0.578	16.01
10	1.45	16.07
20	2.89	16.26
40	5.78	17.01

Table 4.2: Driving frequency and the associated impedance in the z-coil pair for tests of the Centent CN0122 response to various reactive loads.

With the addition of the 1 Ω power resistor, the total impedance over the frequency range only varies from 17 Ω to roughly 18 Ω. As a comparison, in the second set of tests the variable resistor was adjusted to 14 Ω through 18 Ω in 1-Ω steps, and the plots in Figure 4.5 were obtained.

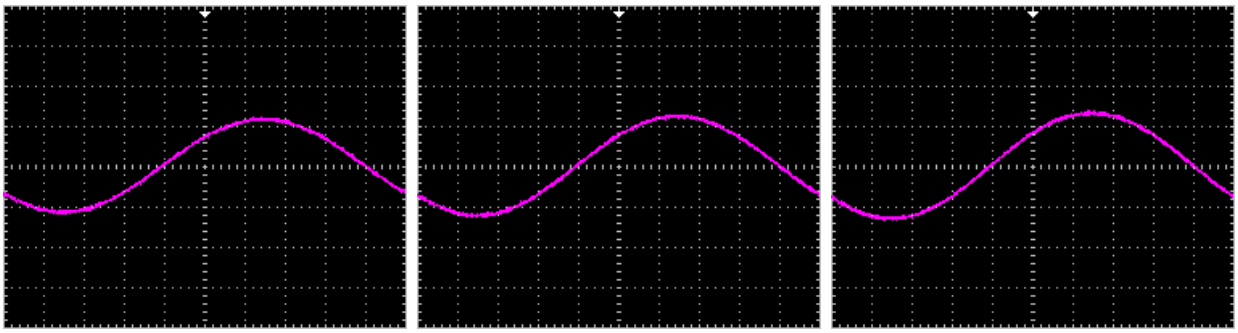

(a) 14 Ω resistance **(b)** 15 Ω resistance **(c)** 16 Ω resistance

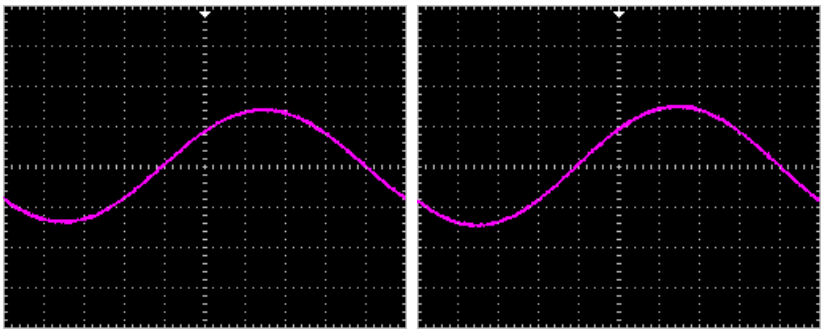

(d) 17 Ω resistance **(e)** 18 Ω resistance

Figure 4.5: Current output of the Centent CN0122 amplifier driving a variable resistor with a function generator sinusoid as its input voltage. Oscilloscope screen captures are shown for variable resistor settings that reflect the total impedances (—Z—) in Table 4.2, plus the addition of a 1 Ω resistor in series. In each image the vertical scale is 5 V per division, and the horizontal scale is 100 ms per division. There doesn't appear to be any current output issues with the amplifier for any of the real resistive loads. This suggests that the amplifier is capable of driving a purely resistive load with no issue, however, it does not respond well to the reactive load of the compensation coil, as shown in Figure 4.4.

The zero-crossing glitch seems to be non-existent in the case of connecting the amplifier to a purely resistive load, indicating that it is the reactive component of the coil impedance which is causing the amplifier output issue. When the amplifier is driving an inductive load, such as a coil, as the frequency of the output increases, so to does the reactive component ωL, and the issue becomes more severe. It can be shown that for a coil of relatively lower inductance, the frequency at which the zero-crossing glitch becomes apparent is relatively higher.

4.3 Combined current output response of the amplifier and power supply

In Section 4.5, the current and field response of the compensation coil set was tested. These tests excluded the use of the Agilent U8002A power supply as well as the Centent CN0122 amplifier, both of which were used during active compensation. To test the response of these two devices, a function generator outputting a 6-Vpp, 200-Hz square wave was connected as the input voltage to the Centent amplifier, and the output was connected across a 1-Ω power resistor. The amplifier was driven by the Agilent U8002A power supply, and a differential voltage measurement was taken across the 1-Ω power resistor. Figure 4.6 shows the experimental setup used to measure the current output. Figures 4.7 and 4.8 show screen captures of the oscilloscope measurement for the test.

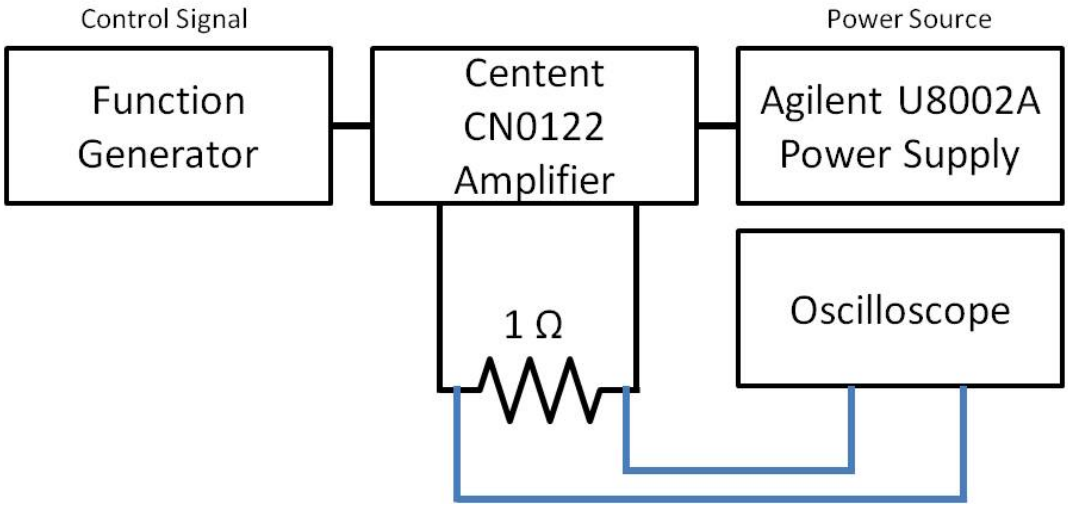

Figure 4.6: Schematic of the experimental setup used to test the current response of the combined Centent CN0122 amplifier and Agilent U8002A power supply.

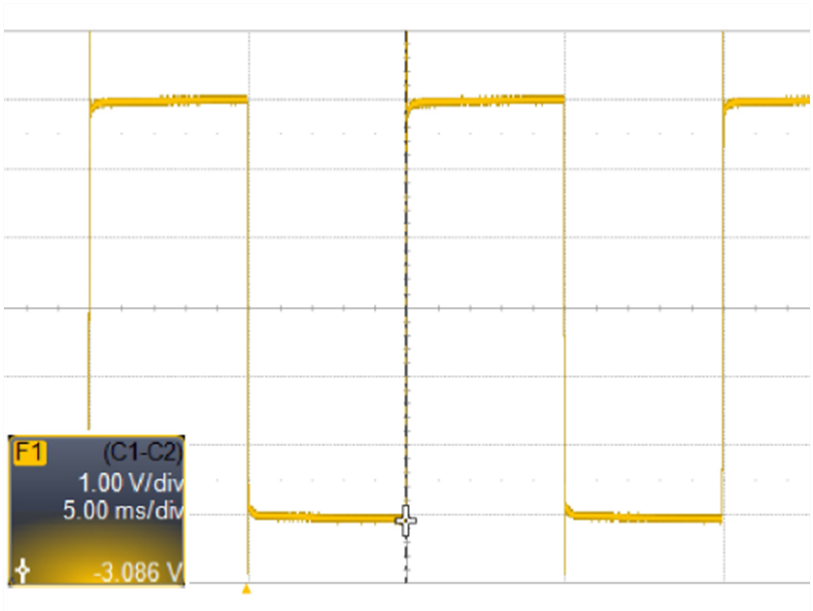

Figure 4.7: Differential measurement of the voltage drop across the 1-Ω power resistor for a current output from the Centent CN0122 amplifier, powered by the Agilet U8002A dc power supply. The amplifier input voltage is from a function generator outputting a 6-Vpp, 200-Hz square wave. The vertical scale is 1 V per division, where each unit volt represents 1 A of current in the output of the Centent CN0122 amplifier. The timescale is 5 ms per division, showing several cycles of the 200 Hz square wave.

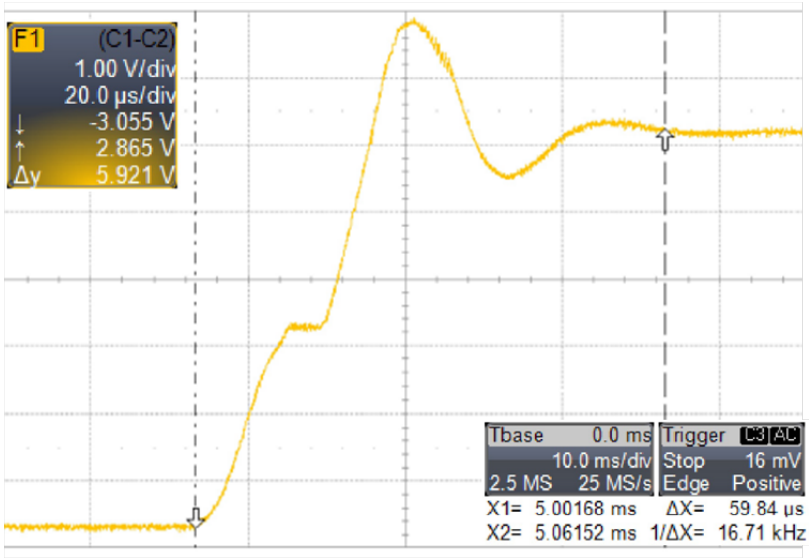

Figure 4.8: Increased timescale resolution for the same voltage measurement as in Figure 4.7. The timescale is 20 μs per division, and only a piece of one cycle of the 200-Hz square wave can be observed. The time-axis cursors are set to measure the points at which the step in voltage begins and ends, taking the settling time into account. The cursor measurement reveals that the step takes slightly less than 60 μs from start to finish.

The result of the measurement is that the Centent CN0122 amplifier driven by the Agilent U8002A

power supply combination can provide current output steps of roughly 6 amps in 60 μs. Dividing the total current by the time provides a measure of the change in current per unit time, as shown in equation 4.3.

$$\frac{6 \text{ A}}{60 \ \mu\text{s}} = 1 \times 10^5 \text{ A/s} \ . \tag{4.3}$$

The amplifier and power supply combination is capable of providing a current change at the rate of 1 $\times 10^5$ A/s when connected across a 1 Ohm purely resistive load.

4.4 Magnetic field and current output

The expected magnetic field output resolution for the combined system of the Bartington fluxgate, NI USB-6215 ADC, and the Centent CN0122 amplifier can be calculated knowing each of the individual device resolutions. For the DAC a value of 320 μV is used to represent the 16-bit coding, the Centent amplifier has a measured slope of 0.9818 A/V, and the x-coil pair has a measured sensitivity of 34.09 μT per Amp of drive current. The calculation is performed as follows:

$$B_x \text{ field resolution} = 0.000320 \text{ V} \times 0.9818 \ \frac{\text{A}}{\text{V}} \times 34.09 \ \frac{\mu\text{T}}{\text{A}} = 10.7 \text{ nT}. \tag{4.4}$$

To measure the current the output of the combined system, a 1-Ω power resistor was connected in series with the x-coil pair and connected to the output of the Centent CN0122 amplifier, drawing its current from the Agilent U8002A power supply. A LabVIEW$^{\text{TM}}$ program was written to output voltage steps of 100 μV to the ADC, which is connected to the voltage input of the Centent amplifier. The voltage drop across the resistor was measured using an Agilent 34411A digital multimeter to log the current running through the coil system, and the fluxgate was used to log the field changes. Figure 4.9 shows a plot of the change in measured magnetic field at the center of the x-coil pair through the course of the voltage steps.

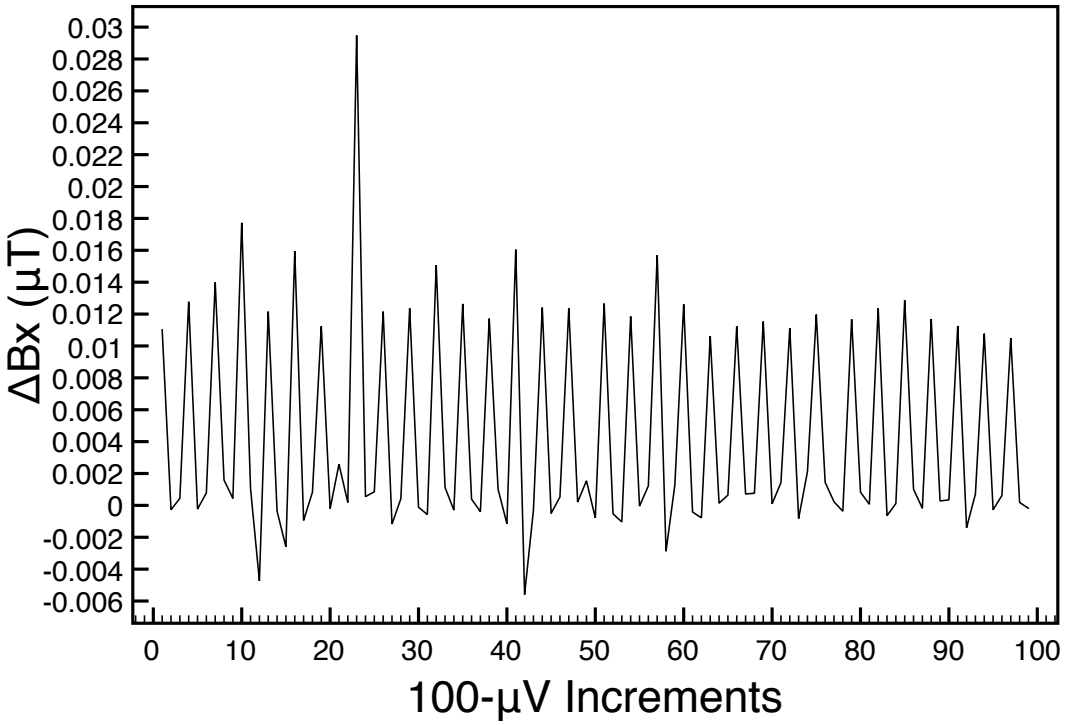

Figure 4.9: Change in the measured magnetic field at the center of the x-coil pair for current steps resulting from 100-μV output steps requested from the DAC. The measured field steps, which correspond to current steps in the coil, occur every three 100-μV increments, on average.

Figure 4.9 shows that the magnetic field changes with roughly every three voltage steps, or every 300 μV output requested from the DAC. Looking closely at the plot you can see that there are a couple of peaks that occur after four voltage steps, rather than three. This is likely attributed to the fact that the actual steps are closer to 320 μV in the DAQs voltage output, as mentioned in Section 3.5. Overall, the measurement confirms the 16-bit resolution of the USB-6215 device. The plot also reveals that the field steps range from $\sim$11 nT to as high as $\sim$30 nT for the step passing through zero. On average they appear to be $\sim$13 nT, which is close to the calculation result in Equation 4.4.

A plot of the current and magnetic field steps resulting from the ADC voltage steps is shown in Figure 4.10 .

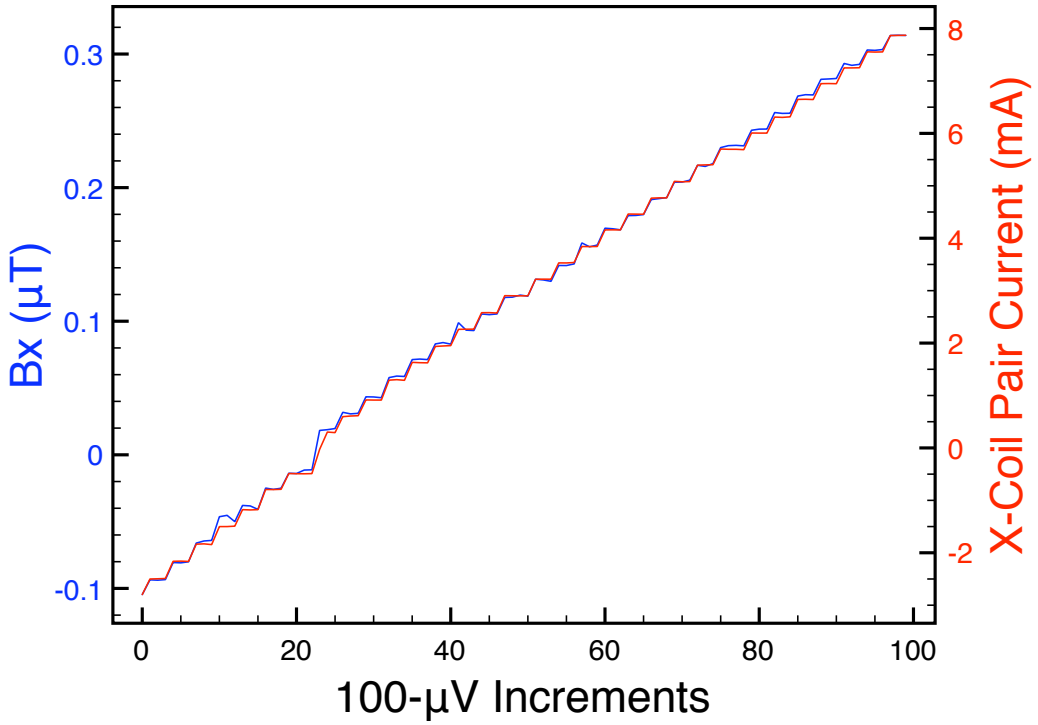

Figure 4.10: Current and field steps resulting from 100 μV voltage step requests to the ADC output.

The plot shows that for each of the current steps, a corresponding magnetic field changed is measured. Figure 4.11 is a higher resolution plot of the current and field steps, showing the similarities between the measured field and current.

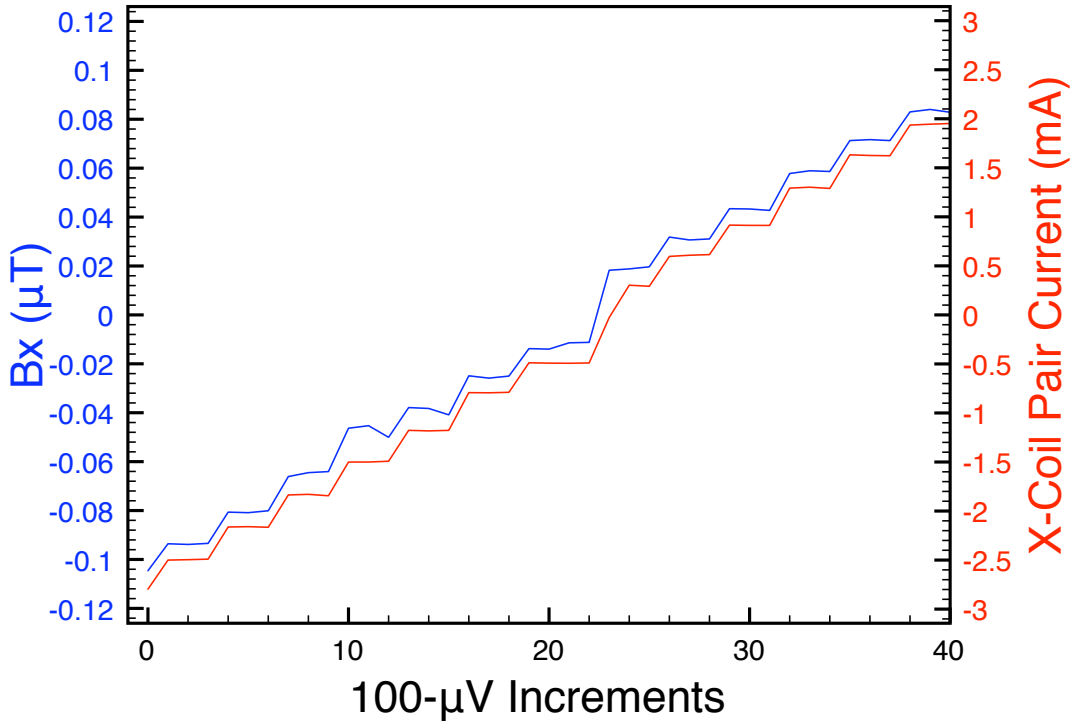

Figure 4.11: Higher resolution plot of the data shown in Figure 4.10.

Excluding the step passing through the zero crossing, each of the current steps in the x-coil pair is roughly 300 nA, with corresponding field steps of roughly 13 nT. You can once again see that each step in the field and current occurs after roughly three data samples, or $\sim$300 μV steps from the ADC output.

4.5 Coil cube current and field response

The windings of each coil are framed on a piece of aluminum u-channel which could potentially impede a rapid increase in applied current through eddy current formation. Each of the x-,y-, and z-coil pairs were analyzed for their response to a rapidly changing applied current by individually connecting each coil in series through a 1-Ω power resistor and a function generator (schematic shown in Figure 4.12). The function generator was set to output a 100 Hz square-wave, and voltage drop across the resistor was measured using an oscilloscope to observe the changes in current in the circuit. Simultaneously, the field output of the coil pair was being monitored by the Bartington

fluxgate, and the output of the Bartington signal conditioning unit was fed to the oscilloscope. Figure 4.13 shows plots of the oscilloscope output for the x-, y-, and z-coil pairs.

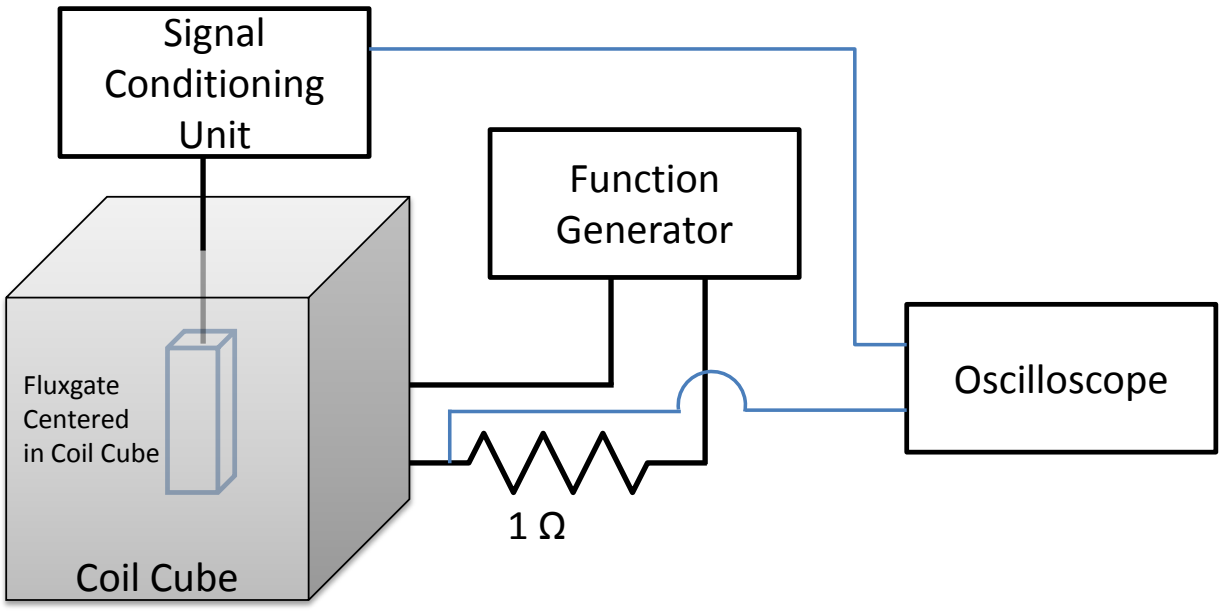

Figure 4.12: Diagram of the experimental setup used to measure the time constant of each coil pair.

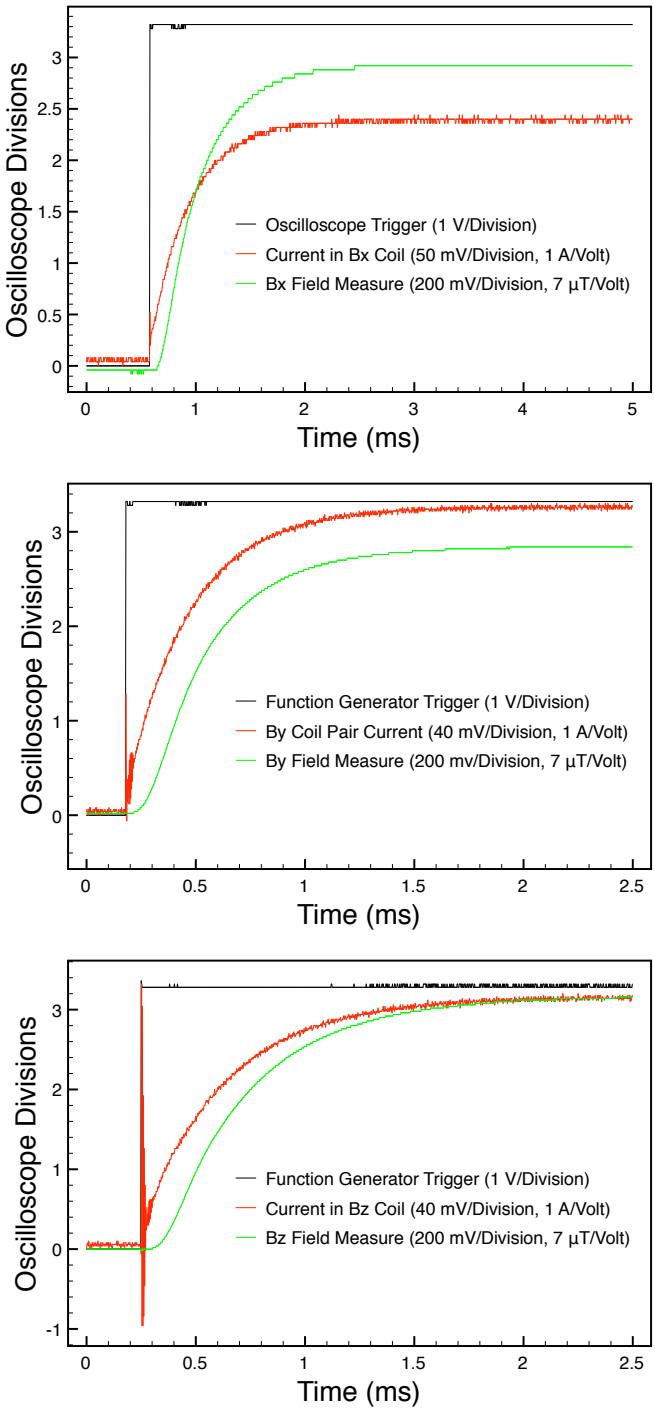

Figure 4.13: Coil pairs driven by a square wave output from a function generator. The plots, from top to bottom, are oscilloscope measurements of the x-, y-, and z-coil pair currents (plotted in red) and resulting fields (plotted in green), for a step in the applied current.

It can be noted from Figure 4.13 that both the current and field increase at an exponential rate. In order to determine the time constant τ for the curves, the exponential portion of each curve was

truncated from the data set and a data fit was performed. The fitting function used was of the form

$$V(t) = A(1 - e^{-t/\tau}), \tag{4.5}$$

where A is the amplitude of the curve, t is the time, and τ is the time constant. Figure 4.14 shows the result of the data fits for each of the x-, y-, and z-coil currents. The data fits for the field measurements are shown in Figure 4.15. The time constant τ for current ramp and associated field measurements in each of the coil pairs are listed in Table 4.3. It is important to note that the value of τ for the current rise in each coil pair is within 3 percent of the associated field rise. This indicates that there is only a small lag between the current driven into the coil and the resulting field produced.

Coil Pair	τ current (μs)	τ of field (μs)
X	370	362
Y	292	288
Z	392	403

Table 4.3: Coil cube current and field time constants taken from the data fits in Figures 4.14 and 4.15.

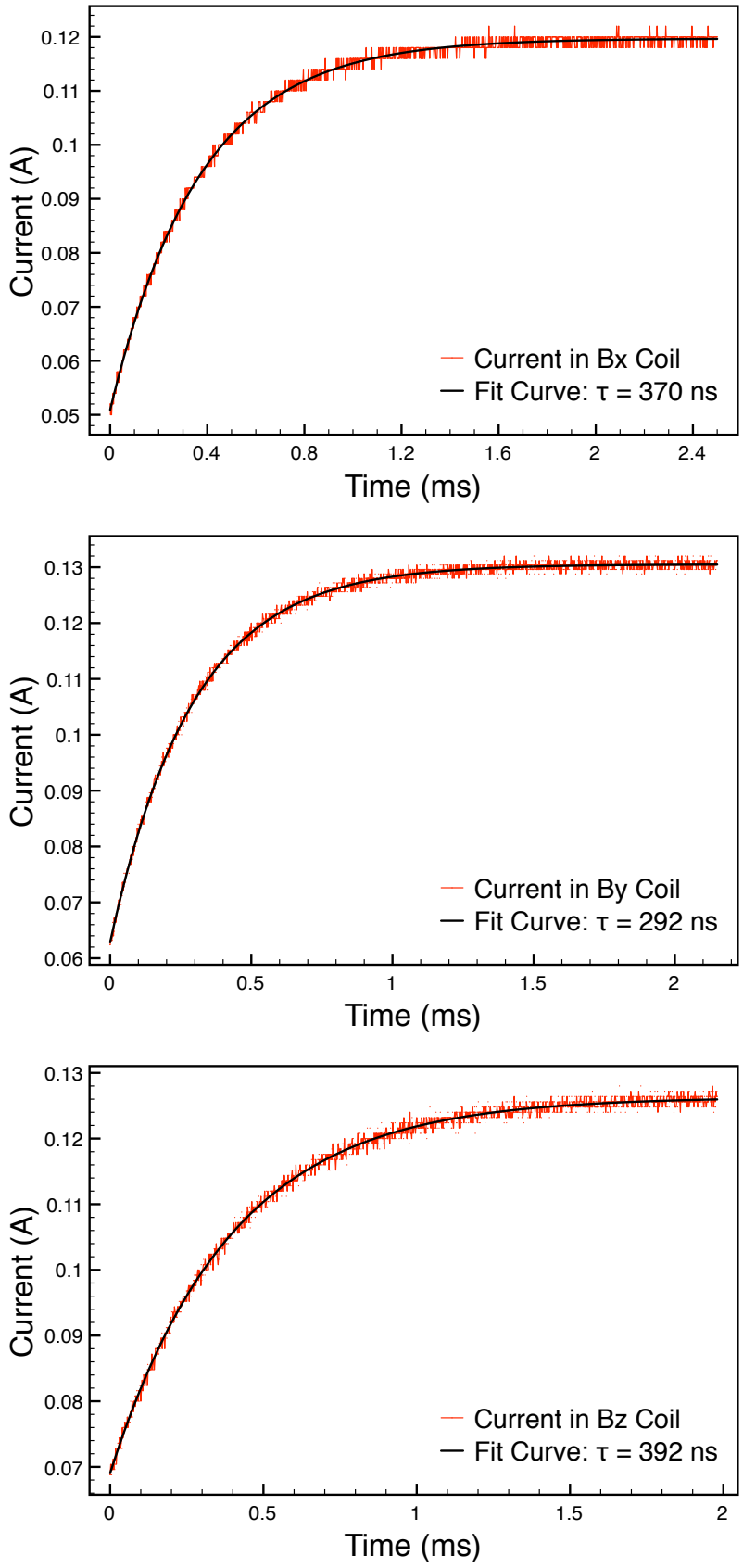

Figure 4.14: Data fits for the exponential portion of the current ramp for each of the x-, y-, and z-coil pairs.

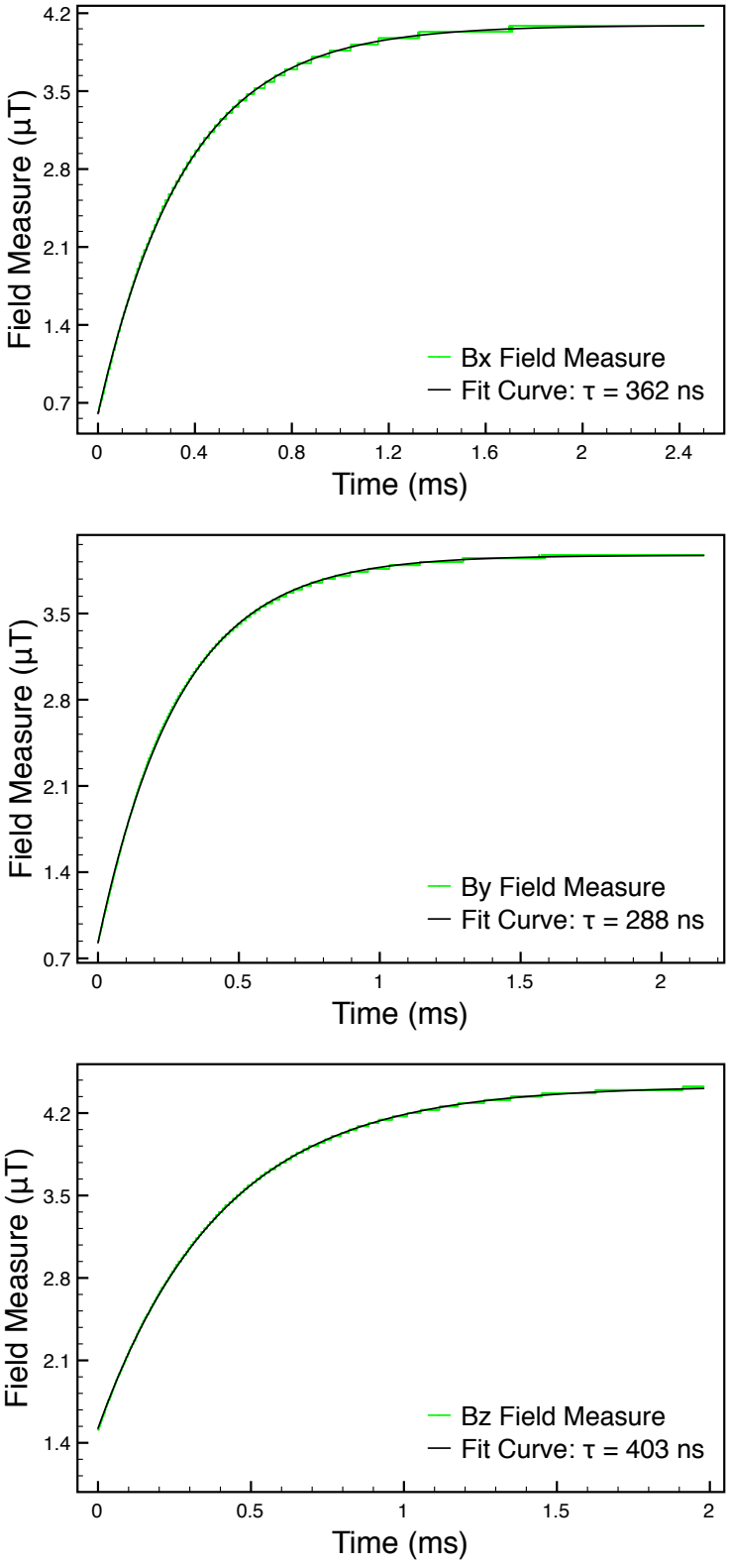

Figure 4.15: Data fits for the exponential portion of the field response for each of the x-, y-, and z-coil pairs.

4.6 Summary of pertinent timescales

A control loop, such as the active magnetic shielding system presented in this work, will have limitations based on the individual elements of the system. In the previous sections of this chapter, the performance of key components of the present active magnetic shielding system were tested to determine possible limitations. The result of the performance tests provides characterization of the components in terms of their timescales for use. Table 4.4 lists the maximum operational frequency bandwidths of the system components. The operating rate of software controller, which sets the field sampling rate of the system, is the slowest element in the field control loop, with a rate of 400 Hz. This will likely limit the maximum perturbation frequency that can be actively shielded, as well as the reduction in field amplitude achieved for any perturbation. The next limiting operating frequency, after the software controller, is set by both the fluxgate frequency response and the coil cube current response. These are both limited to 1000 Hz, which provides room for improvement on the software controller rate before any adjustments are required for the fluxgate or coil cube. Finally, the combined power supply and amplifier can easily operate at 16000 Hz, which is well above any other timescale of the active shielding system and will not pose an issue unless the operating rate of the other components are increased significantly.

System component	Bandwidth (Hz)
Controller rate	400
Fluxgate response	1000
Coil cube response	1000
Amp/ps I output	16000

Table 4.4: Operational bandwidths of the active magnetic shielding system components.

Chapter 5

Analysis and results

The previous chapter described the performance of each of the active shielding system components. In this chapter, the performance of system as a whole will be shown using the results of a series of shielding factor tests. The goal is to characterize the active shielding ability of the system by performing shielding tests with a variety of perturbation amplitudes and frequencies present, as well as varying the field sampling rate of the system. A method to reduce the background field will also be introduced, and shielding tests will be performed to determine the effectiveness of the method. Before the tests of system performance are shown, the background fields in the laboratory will be briefly examined, and the method used to determine the effectiveness of the active shielding will be described.

5.1 Characterization of background fields

Background ac magnetic fields in the region of the fluxgate sensor could interfere with the ability to perform active magnetic shielding. As previously mentioned, the sampling rate of the present system is limited to ∼400 Hz, which effectively filters the magnetic field measurement to frequencies below this limit. If the active shielding is only found to be effective on ac fields up to a fraction of the sampling rate limit, then background ac fields of frequencies outside the active shielding range will not be reduced. If the frequency of such fields are below ∼400 Hz, then they will remain in the field measurement while attempting to perform active shielding. A frequency analysis was performed to

determine the spectrum of the background magnetic field in the laboratory environment.

The z-axis fluxgate sensor was used to perform the background field measurement. The unconditioned output of the SCU was connected to an oscilloscope with a built in spectrum analyzer, and the frequency spectrum was measured. The measurement was performed at different times on different days of the week to observe the change in the background magnetic field spectrum. Figures 5.1, 5.2, and 5.3 show the spectrum analyzer output up to 500 Hz.

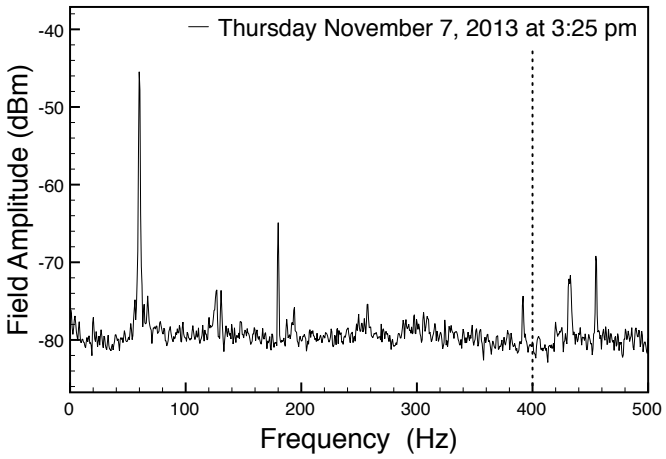

Figure 5.1: Background magnetic field spectrum, mid-afternoon on a typical weekday. The two dominant peaks below are $\sim$ 35 dBm at 60 Hz and $\sim$ 15 dBm at 180 Hz. The dashed line at 400 Hz indicates the typical maximum sampling frequency achievable with the present prototype active shielding system.

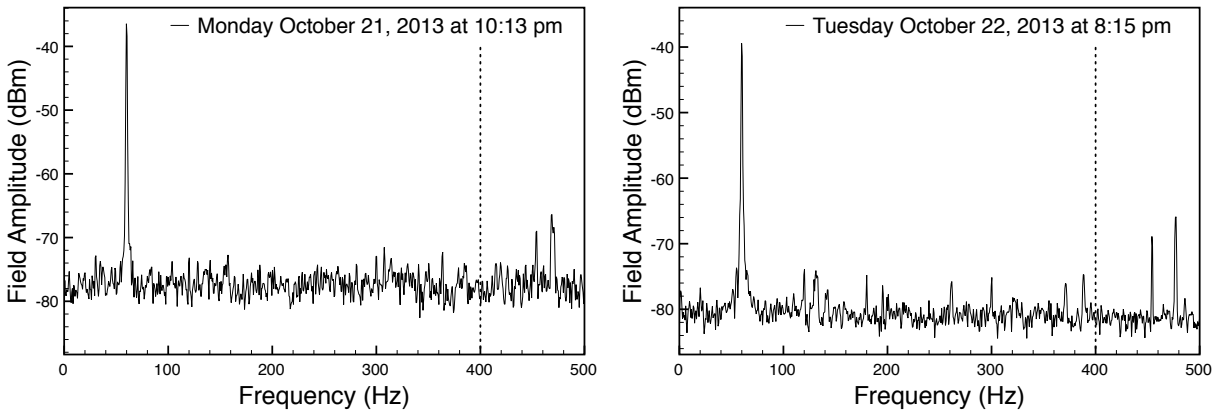

Figure 5.2: Background magnetic field spectrum on two consecutive weekday evenings. Below 400 Hz a single dominant peak of $\sim$ 40 dBm is observed at 60 Hz. The dashed line at 400 Hz indicates the typical maximum sampling frequency achievable with the present prototype active shielding system.

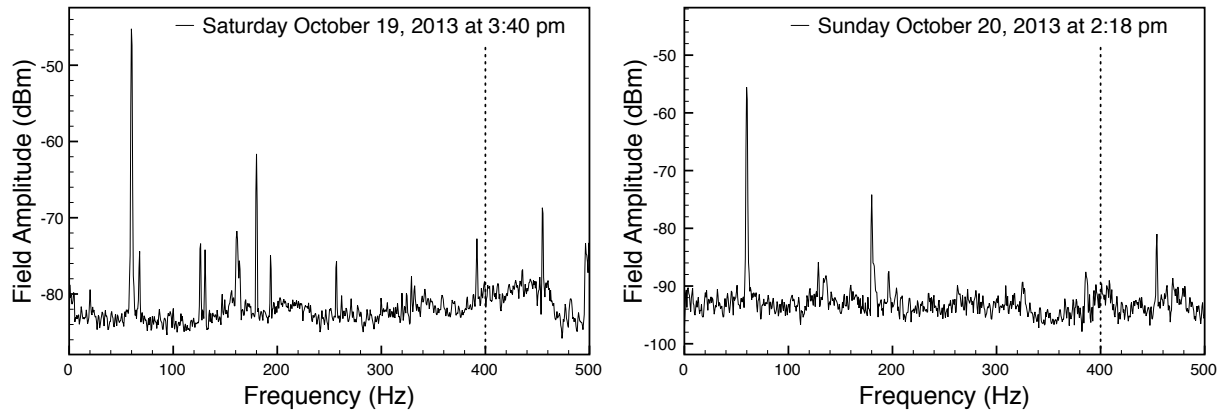

Figure 5.3: Background magnetic field spectrum on Saturday and Sunday afternoon of the same weekend. The spectrum from Saturday shows two dominant peaks below 400 Hz: $\sim$ 38 dBm at 60 Hz and $\sim$ 22 dBm at 180 Hz. There are also several smaller peaks at various frequencies. The spectrum from Sunday shows two dominant peaks below 400 Hz: $\sim$ 38 dBm at 60 Hz and $\sim$ 20 dBm at 180 Hz. The dashed line at 400 Hz indicates the typical maximum sampling frequency achievable with the present prototype active shielding system.

The background magnetic field frequency spectra show that the dominant signal is a 60-Hz field in the laboratory at all times. There is also a peak at 180 Hz (a harmonic of 60 Hz) during the daytime. This is an expected result as the ac power line frequency in the laboratory is 60 Hz. It stands to reason that this environmental noise may interfere with the ability to actively shield magnetic fields in the laboratory when a sampling rate of 400 Hz is used. At the end of this chapter, a method to reduce the 60-Hz background will be explored and tests of the system performance using the method will be shown.

5.2 Shielding factor calculation

The shielding factor (SF) of the active shielding system was determined by applying a sinusoidal magnetic field perturbation $Bsin(2\pi ft)$, and comparing the total field magnitude with and without the active shielding enabled (as shown in Equation 5.1 where off and on refer to the state of the active shielding system). Henceforth, the actively shielded perturbation will be referred to as a residual field.

$$SF = \frac{B_{off}^{tot}}{B_{on}^{tot}} \tag{5.1}$$

The first calculations of the shielding factor were performed using the peak-to-peak values of the perturbation and residual fields. This was achieved by taking the difference between the maximum and minimum values in each set of measured field data. The issue with this method stems from the significant difference in the signal-to-noise ratio (SNR) of each data set. The unshielded perturbation has a high SNR, providing an accurate measure of the peak-to-peak amplitude by taking the difference between the maximum and minimum values of the data. The residual data SNR is low by comparison, and attempting to measure the amplitude in the same manner as the unshielded data gives unreliable results dominated by background noise, zero-crossing spikes from the amplifier, as well as other transient fields. This can be seen in Figure 5.4, which shows plots of an applied magnetic field perturbation and the residual field resulting from active shielding.

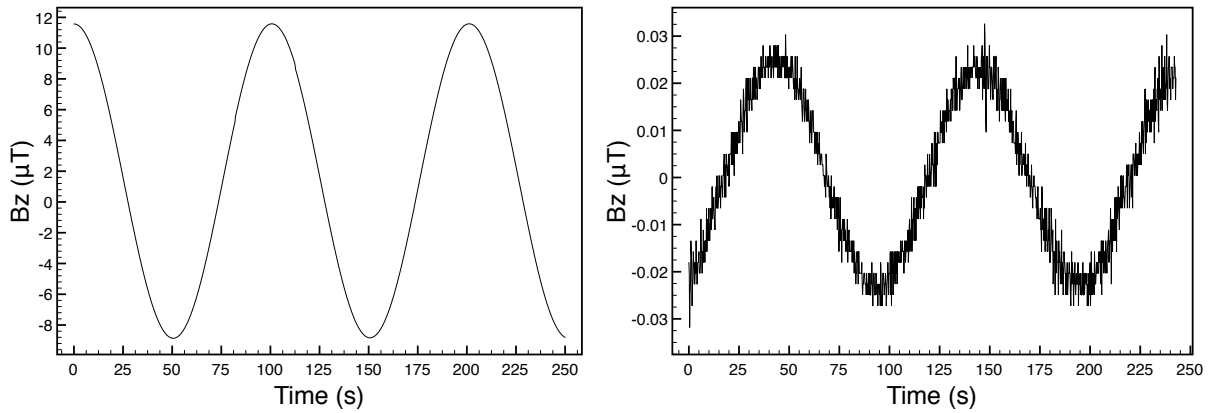

Figure 5.4: Comparison of a magnetic field perturbation and its residual field after active shielding is applied. (a): Measurement of an unshielded, applied sinusoidal field perturbation. (b): Measurement of the residual applied sinusoidal perturbation with active shielding.

Another method to compare the perturbation and residual fields used a data fit for each of the fields. The amplitudes taken from the data fits were used to calculate a shielding factor. In this case, the data fit for the uncompensated sinusoid was very precise with little error. The error in the data fit for the residual field, however, was much larger than for the unshielded perturbation, due to the difference in SNR. This resulted in an unreliable value for the shielding factor once the quotient of the fit amplitudes was calculated. Suppose that the active shielding is capable of driving the residual field into the background noise, resulting a an SNR of zero. A best fit of the noise

would be a straight line, or a sinusoid of zero amplitude. This would result in an erroneously large shielding factor.

The method which was finally chosen to determine the shielding factor was a calculation of the root-mean-square (RMS) value for one period each of the perturbation and residual fields. The RMS value is calculated using the following formula:

$$X_{RMS} = \sqrt{\frac{\sum_{i=1}^{n} x_i^2}{n}}, \tag{5.2}$$

where x_i are the field measurement values in the data, and n is the number of values in the set. The shielding factor is then:

$$SF_{rms} = \frac{(B_{rms}^{tot})_{off}}{(B_{rms}^{tot})_{on}}. \tag{5.3}$$

Since this calculation includes averaging over an entire cycle of data, it solves the issues associated with a peak-to-peak or data fit method. In section 5.3, all calculations of shielding factors will be ratios of the RMS value for one cycle each of the perturbation field and residual field data, and will be referred to as RMS shielding factors.

5.3 Results of system performance

In order to understand the behavior of the feedback system and to characterize the performance, several shielding tests were performed. These tests provide information about the limitations of the overall active shielding ability of the present system, and provide critical information for building a better system. The shielding tests were performed in the vertical direction (z-axis), which is subject to the largest dc background magnetic field.

5.3.1 Sampling rate and its effect the on shielding factor

The first test of the performance of the active shielding system was to determine the maximum perturbation frequency that can be effectively shielded when operating at a fixed sampling rate.

The goal of this test is to determine the relationship between the perturbation frequency and sampling rate, relative to the achievable shielding factor. The test was performed by applying a 124 μTpp sinusoidal perturbation to the active shielding region, which is sufficiently strong to explore a large range of shielding factors. The field sampling rate and perturbation frequency were fixed, and a shielding test was performed. The perturbation frequency was then increased and another shielding test was performed. Once a shielding factor was obtained for the chosen set of perturbation frequencies at the present field sampling rate, the sampling rate was increased and the same range of perturbation frequencies was repeated. The low-pass filter on the signal conditioning unit was set to 1 kHz for the entire set of tests.

The maximum perturbation frequency applied for each sampling rate was chosen to be the frequency at which the RMS shielding factor dropped below unit. A shielding factor of 1 indicates that the active shielding is no long effective, and shielding factors below 1 indicate that the residual field is larger than the unshielded perturbation. The test was performed over a range of perturbation frequencies from 10 mHz up to 50 Hz, and a sampling rate range of 1 Hz up to 400 Hz. The results are displayed in Table 5.1, and plots of these results are shown in Figures 5.5 and 5.6.

	Sampling Rate (Hz)										
$\mathbf{f_{perturbation}}$ **(Hz)** $\downarrow$	**1**	**2**	**5**	**10**	**20**	**30**	**50**	**100**	**200**	**300**	**400**
0.01	16	32	81	244	374	568	670	568	708	1068	1068
0.02	8.1	16	41	126	202	278	417	563	630	1000	1050
0.05	3.3	6.5	16	51	83	117	191	350	492	818	887
0.1	1.6	3.3	8.1	25	42	58	98	190	312	529	589
0.2	<1	1.7	4.1	13	21	29	50	98	175	297	328
0.5		<1	1.6	5.1	8.3	12	20	40	74	121	135
1			<1	2.5	4.2	5.9	10	20	37	62	69
2				<1	2.1	2.9	4.9	10	18	31	35
5					<1	1.1	1.9	3.9	7.4	10	14
10						<1	<1	1.9	3.6	6.3	6.9
20								<1	1.7	2.9	3.2
50									<1	<1	<1

Table 5.1: RMS shielding factors obtained for combinations of perturbation and sampling frequencies while maintaining a fixed perturbation amplitude of 124 μTpp.

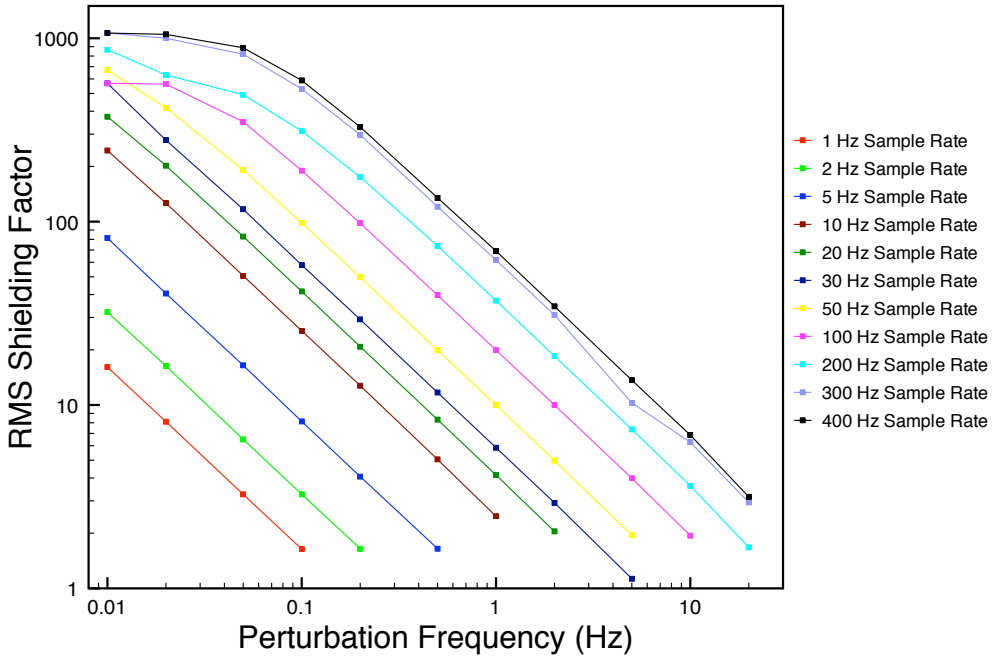

Figure 5.5: Plot of the RMS shielding factor vs the frequency of the applied perturbation. The series of data, indicated by the solid lines connecting the data points, corresponds to a fixed sampling rate of the system. The plot shows that the shielding factor is inversely proportional to frequency of the applied field perturbation.

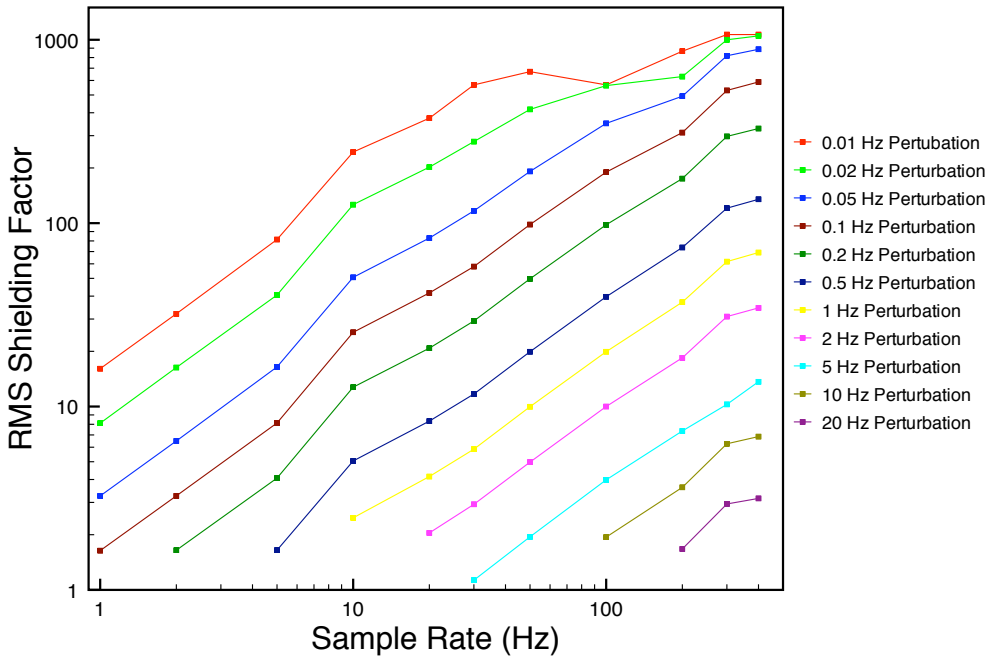

Figure 5.6: Plot of the RMS shielding factor vs the sampling rate of the system. The series of data, indicated by the solid lines connecting the data points, corresponds to a fixed frequency of the applied perturbation. The plot shows that the shielding factor is linearly proportional to the field sampling rate of the system.

The results shows a well defined trend. There is a direct relationship between the sampling rate of the system and the shielding factor at specific perturbation frequencies. In general, the shielding factor obtained is linearly proportional with the sampling rate of the system and inversely proportional with the frequency of the applied field perturbation. As the sampling rate of the system is increased for a fixed perturbation frequency, the shielding factor increases. As the perturbation frequency is increased for a fixed sampling rate, the shielding factor decreases.

As mentioned previously, a shielding factor of unity or less indicates that the system is not providing any measurable active shielding. Table 5.1 shows that for each sampling rate, the maximum perturbation frequency which can be actively shielded is one tenth of that frequency. Since the sampling rate of the system can not exceed ∼400 Hz, the maximum perturbation frequency that can be actively shielded is ∼40 Hz. However, the shielding factors obtained for frequency ratio is not adequate for any experiments requiring a reasonably quiet magnetic field environment. For example, to achieve a shielding factor of ∼ 100 for perturbations below 0.5 Hz, a sampling rate of 500 times the perturbation frequency is required using the present system. The two highest shielding factors obtained for the series of tests are the same value of 1068, as seen in Table 5.1. This results from the residual field being driven into the noise floor of the background field, and will be further examined in the following section.

5.3.2 Perturbation amplitude and its effect on the shielding factor

The second test of system performance was to observe how the amplitude of the applied perturbation affects the active shielding. For this set of tests, the operating frequency of the system was fixed at 300 Hz and the sinusoidal perturbation frequency was set to values ranging from 10 mH to 1 Hz. For each of the perturbation frequencies, the perturbation amplitude was adjusted through values ranging from ∼1 μTpp to ∼124 μTpp. For each perturbation amplitude, the active shielding was engaged and a shielding factor was obtained. Once again, the low-pass filter was set to 1 kHz for this set of tests. Table 5.2 shows the results of the test, which are plotted in Figure 5.7.

	Perturbation Frequency (Hz)				
$A_{perturbation}$ (μT) $\downarrow$	**0.01**	**0.1**	**0.2**	**0.5**	**1**
1.4	12.9	14.4	14.7	13.3	13.9
2.7	26.3	32.1	30.5	26.7	25.7
6.5	71.9	83.2	71.4	55.9	50.4
12.9	141	144	133	92.8	61.2
25.7	262	309	208	109	54.9
63.2	662	500	271	113	66.5
124.4	1218	542	335	122	65

Table 5.2: RMS shielding factors for different perturbation amplitudes and frequencies with a fixed field sampling rate of 300 Hz.

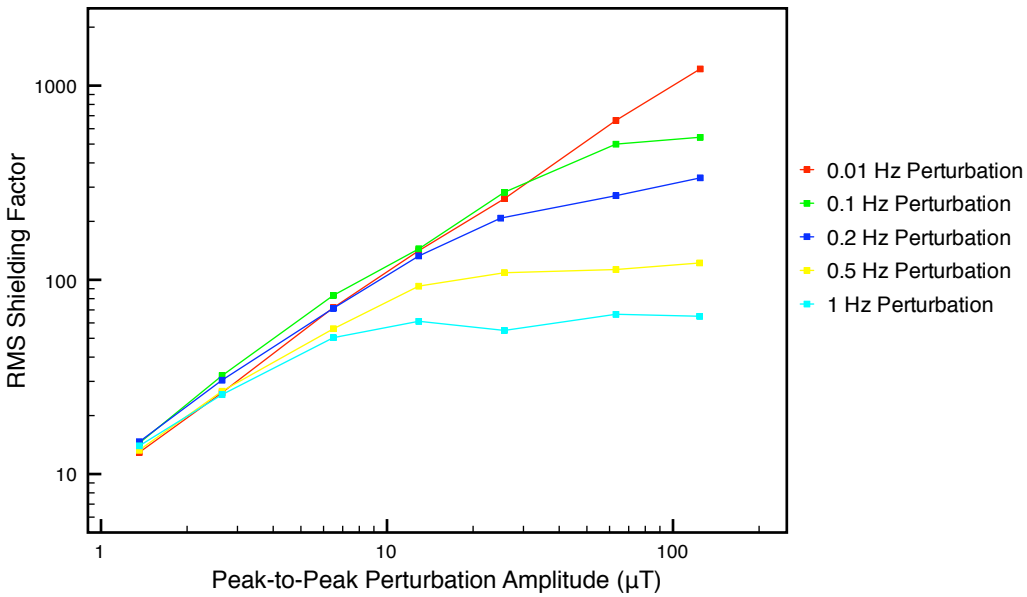

Figure 5.7: Plot of the RMS shielding factor obtained for different perturbation amplitudes and frequencies with a fixed field sampling rate of 300 Hz. The plot shows that the shielding factor obtained is proportional to the perturbation amplitude, for combinations of low frequency and low amplitude perturbations. For combinations of higher amplitude and frequency perturbations, the shielding factor is independent of the perturbation amplitude.

Figure 5.7 shows that for the lowest perturbation frequency of 0.01 Hz, the shielding factor

obtained is proportional to the perturbation amplitude. For the perturbation frequencies above 0.01 Hz, the shielding factor is proportional to the perturbation amplitude up to a cutoff. The perturbation amplitude at which the cutoff occurs is lower for each perturbation frequency, in ascending order. Inspection of the residual data for the 0.01 Hz perturbation (shown in Figure 5.8) reveals that the compensation system is driving the residual field into the noise region of the laboratory background field. The result is a limit to the residual field amplitude at the level of background noise floor, which explains why the shielding factor obtained for the 0.01 Hz perturbation increases in proportion with the perturbation amplitude. Each increase in the perturbation amplitude yields the same residual field, which is the background noise level, and therefore any increase in perturbation amplitude yields a proportional increase in the shielding factor.

Figure 5.8 shows a side-by-side comparison of the residual fields for three different perturbation amplitudes (1.4 μTpp, 63.2 μTpp, and 124.4 μTpp) at two perturbations frequencies (0.01 Hz and 1 Hz). The comparison shows that the residual fields from the 1 Hz perturbation behave differently than those from the 0.01 Hz perturbation. For the 1.4 μTpp, 1 Hz perturbation, the residual field is driven into the noise floor of the background field, as with all residual fields for the 0.01 Hz perturbation. The higher perturbation amplitudes, however, yielded residual fields much larger than the noise floor, which explains why the shielding factor scaled differently for the 1 Hz perturbation and the 0.01 Hz perturbation. As the perturbation amplitude and frequency increase, the system can no longer adjust the field output rapidly enough to compensate for the increase in perturbation field per unit time, and therefore can not drive the field into the noise floor of the laboratory. Once this begins to occur, the shielding factor becomes independent of the perturbation amplitude.

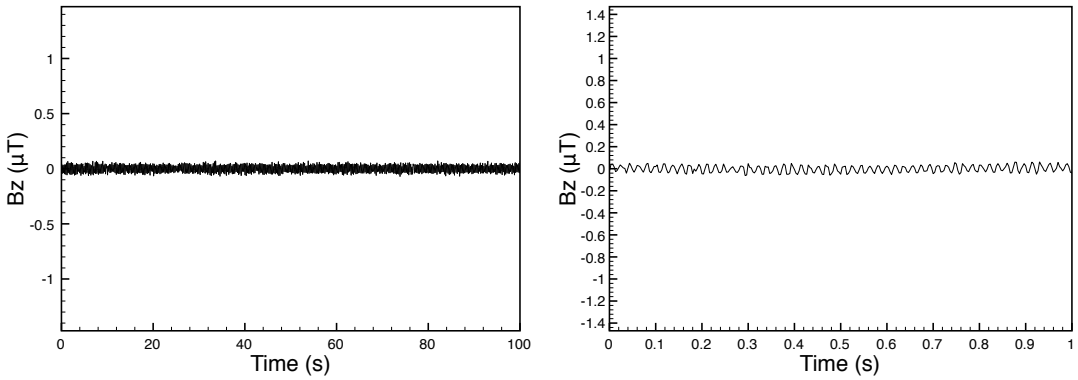

(a) 1.4 μTpp, 0.01 Hz perturbation

(b) 1.4 μTpp, 1 Hz perturbation

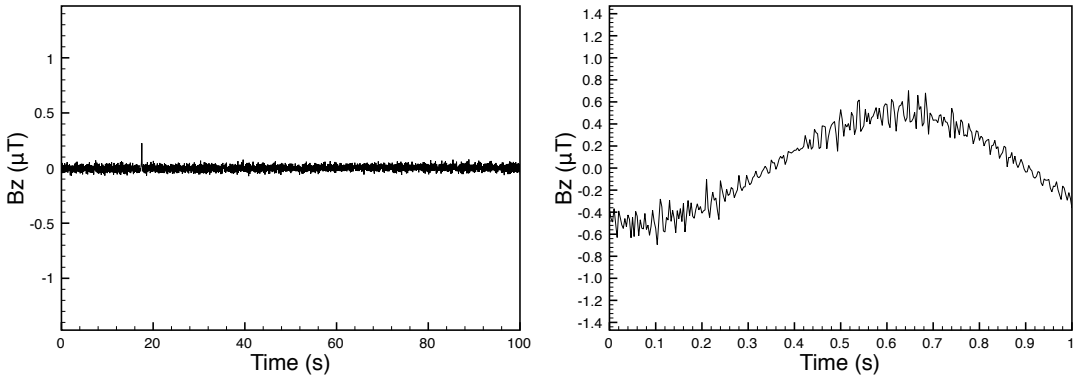

(c) 63.2 μTpp, 0.01 Hz perturbation

(d) 63.2 μTpp, 1 Hz perturbation

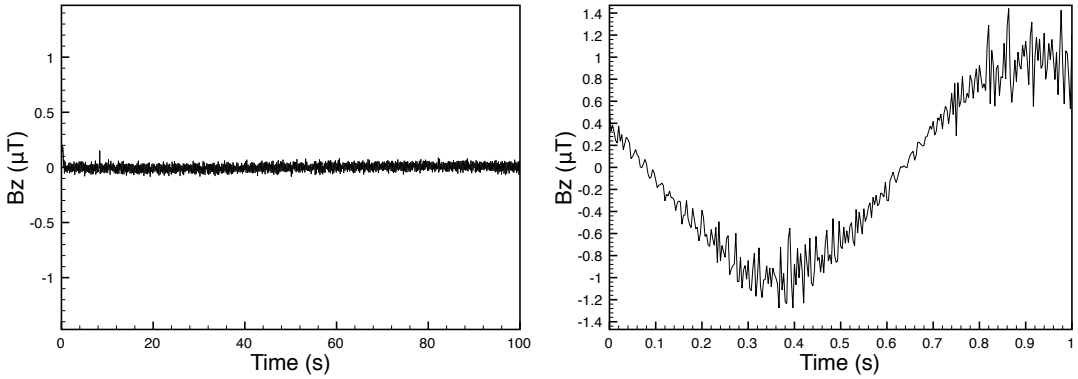

(e) 124.4 μTpp, 0.01 Hz perturbation

(f) 124.4 μTpp, 1 Hz perturbation

Figure 5.8: Side by side comparison of the residual field measurements for two different perturbation frequencies and three different amplitudes. From top to bottom, the three rows are plots of the lowest (1.4 μTpp), middle (63.2 μTpp) and highest (124.4 μTpp) perturbation amplitudes. The left column are residual fields for the 0.01 Hz perturbation, and the right column is for the 1 Hz perturbation. The plots of the 0.01 Hz perturbation residual fields remain buried in the noise floor up to the highest perturbation amplitude, where the sinusoidal shape is just beginning to show. The first plot of the 1 Hz perturbation is mostly buried in the background noise floor, however, as the perturbation amplitude increases, the residual field leaves the background noise and the sinusoidal shape of the perturbation becomes apparent.

Since the lower frequency and amplitude perturbations are driven into the background noise, one of the limiting factors for reducing the field amplitude of low-frequency perturbations is the magnitude of the noise floor. It was shown in section 5.1 that the dominant frequency of the background noise in the laboratory is 60 Hz, which is too high for the system to actively shield with its present sampling rate limit (as shown in Section 5.3.1). By specific reduction of the 60 Hz noise, the shielding factor for the lower frequency perturbations should increase.

5.3.3 60 Hz bucking and its effect on shielding factor

The dominance of the 60-Hz frequency in the background field (shown in section 5.1) lead to the idea of a specific 60-Hz cancellation coil. Since this is the line frequency of the of the power sources in our laboratory, we attempted to use the very same power line signal to perform the cancellation. A small plastic formed coil, wired in series with a 100 kΩ resistor, was connected to the 60-Hz, 120-volt laboratory ac power line (schematic shown in Figure 5.9), and was used to cancel, or buck, the 60 Hz background noise.

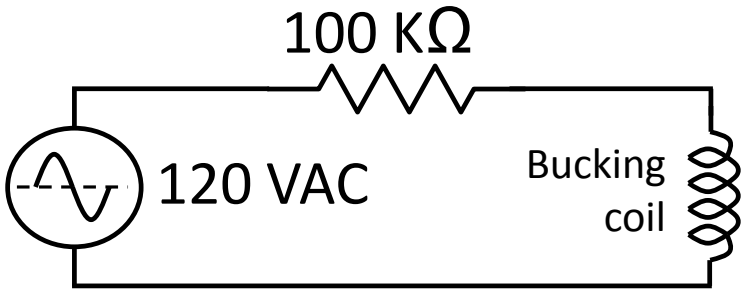

Figure 5.9: Schematic of the apparatus used for 60 Hz bucking of the background field.

By placing the bucking coil in the vicinity of the fluxgate sensor and adjusting its position carefully, the 60-Hz background noise can be reduced significantly, as shown in Figure 5.10. It is also possible to increase the 60-Hz background noise by changing the orientation of the coil 180° relative to the fluxgate sensor. In this configuration, the bucking coil position can be adjusted to increase the 60-Hz background by different amounts.

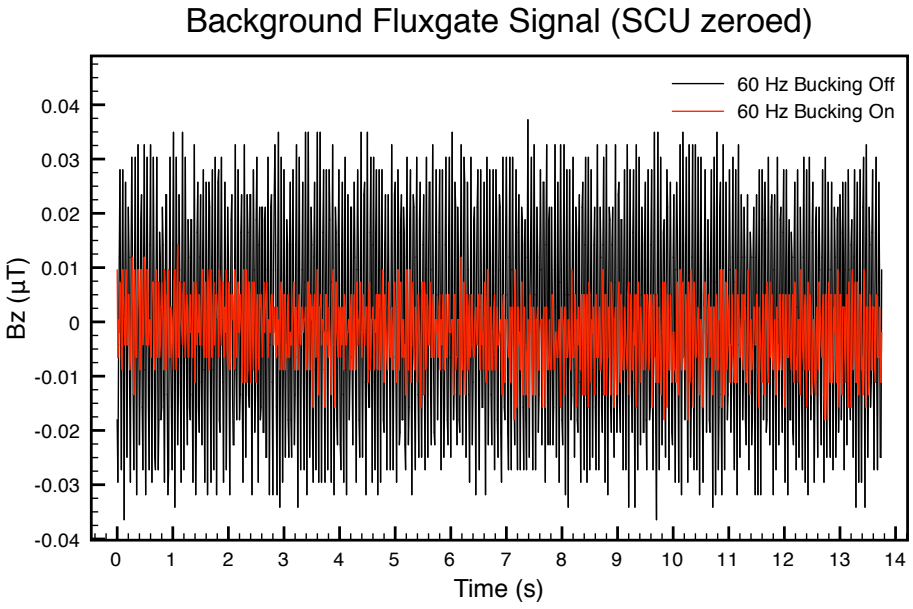

Figure 5.10: Background field measurement sampled at 400 Hz with (red data) and without (black data) the 60-Hz bucking coil in place. The use of the bucking coil produces a significant decrease in the amplitude of the field measurement.

As mentioned previously, the bucking coil can be used to increase or decrease the 60-Hz background, however, it should be mentioned that it is not possible to reduce the 60-Hz background to zero. To test the effect of the 60-Hz bucking on the shielding factor, active shielding measurements were taken with varying degrees of 60-Hz background noise, both below and above the normal level. For each test, the sampling rate was fixed at 400 Hz, the perturbation frequency was fixed at 0.1 Hz, and the perturbation amplitude was fixed at 69.6 μTpp. Prior to each test, the 60-Hz bucking coil was set in place near the fluxgate sensor and adjusted until the desired level of 60-Hz signal was achieved. The peak-to-peak 60-Hz background noise was noted and an active shielding test was performed. The results are shown in Table 5.3 and plotted in Figure 5.11.

60 Hz background (nTpp)	42.5	50.4	63.8	73.5	82.6	92.4
RMS SF	571	553	540	503	474	465

60 Hz background (nTpp)	108	112	122	132	143	153
RMS SF	452	442	391	376	352	348

Table 5.3: Shielding factors obtained with different amplitudes of 60-Hz background. The 92.4 nTpp 60-Hz background is a baseline measurement taken on a typical weekday afternoon.

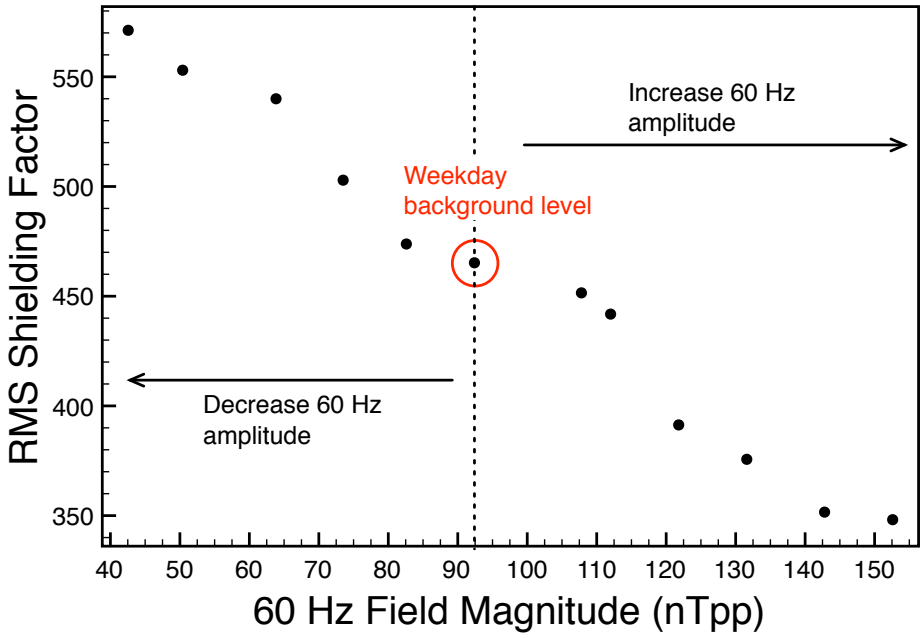

Figure 5.11: Shielding factors obtained with varying levels of 60-Hz background. The low-pass filter was set to 10 kHz and the field sampling rate was fixed at 400 Hz. The perturbation used was 0.1-Hz, 69.6-μTpp. As the 60-Hz amplitude departs from the weekday background level, the shielding factor changes. Lower 60-Hz background results in a higher shielding factor, and higher 60-Hz background results in a lower shielding factor.

The results show that as the 60-Hz component of the background field is reduced or increased, the shielding factor increases or decreases, respectively. In fact, a decrease of ~50 nT to the 60-Hz component of the background field results in an increase of ~100 to the shielding factor. Specific reduction of the 60-Hz noise lowered the total background field dramatically, resulting in better active shielding.

Chapter 6

Conclusions and future work

6.1 Conclusion

A prototype active magnetic shielding system was developed and tested. I characterized the active shielding system by performing a variety of shielding tests, and in doing so, I identified key features and limitations of the performance. The system is capable of providing RMS shielding factors $>$ 1000 for magnetic field perturbation frequencies $\leq$ 20 mHz, and $>$ 100 for frequencies $\leq$ 0.5 Hz, and can reduce magnetic field variations on the order of tens of μT to the level of tens of nT. I conclusively demonstrated that the limiting time constant of the system is the field sampling rate, which is restricted to $\sim$400 Hz by the software controller. A method to reduce the 60-Hz background field was introduced, and was shown to positively affect the active shielding of by improving the signal-to-noise ratio of the residual fields. Over the range of parameters studied, 3 conclusions can be made about the active shielding system:

1. Shielding factor $\propto$ sampling frequency

2. Shielding factor $\propto$ (perturbation frequency)$^{-1}$

3. Shielding factor is ultimately limited by the broadband noise of the background

6.2 Future work

The prototype active shielding system developed in this work is likely the first iteration of many, which will lead to the final system used for the nEDM experiment at TRIUMF. Several factors were not taken into account in its design including passive shield interactions and the placement of the fluxgate sensor relative to the actively shielded region of interest. The prototype passive magnetic shields currently being tested at the University of Winnipeg provide the opportunity to test the active shielding interaction. Placement of field sensors outside the active shielding region of interest will also be examined using recently acquired magneto-resistive field sensors, which are smaller than the 3-axis fluxgate used in this work.

Thus far, the primary limitations of the system are the sampling rate of magnetic fields in the controlling software, and the background noise level in the laboratory. One way to possibly improve the sampling rate of the system is through the implementation of a field programmable gate array (FPGA) to replace the present PC based controller. An FPGA provides the ability to program an integrated circuit directly with the desired code. If the controlling software of the present system were coded onto an FPGA, the result would effectively be a processor that only concerns itself with calculating the error and PID output for current adjustments in the coil set.

By contrast, the LabVIEW^{TM} code used in the present system runs in the foreground of the operating system of the PC. The PC processor performs numerous tasks simultaneous to running the LabVIEW^{TM} code and this spreads out the computing power, potentially slowing down the control loop. National Instruments produces software that is capable of programming existing LabVIEW^{TM} code onto an FPGA, which can then be combined with a DAQ into a single system. This would not only increase the frequency of the control loop software, but also increase the transfer rate between the DAQ and the controller by eliminating the USB connection. Such a system could easily support numerous field measurements and current calculations simultaneously, providing the opportunity to control the magnetic field in multiple axes.

By increasing the sampling frequency of active shielding, the limitations of other system components will eventually become an issue. Table 4.4 shows that the next frequency limit to come

after the 400 Hz sampling rate of the system is the 1000 Hz limit of both the fluxgate frequency response and the coil cube current response. Magneto-resistive field sensors with higher bandwidth than the present fluxgate are already being tested at the University of Winnipeg to solve the first issue. As for the coil cube frequency limit, the inductance must be reduced in future designs to allow for a faster current response. This could be accomplished by reducing the area or number of turns in the coils, or simply separating the coil pairs into individually controlled single coils. The use of unpaired coils, each with their own field sensor, could provide other benefits such as gradient field control.

It was shown that the use of an external bucking coil can reduce the background noise in the active shielding environment, resulting in higher shielding factors. Supposing the 60-Hz noise, or other background frequencies are not of concern to the nEDM experiment, it may still be of benefit to disburden the active shielding system by removing certain frequencies from the field measurement. A notch filter could be the solution, selectively filtering specific frequencies of the field measurement without affecting the frequencies of interest.

The issues revealed with the current amplifier, such as the zero-crossing glitch, led to investigation of specially designed power supplies and amplifiers which will be tested in the next iteration of the active shielding system. These devices will provide higher resolution and better stability for the current driven into the coil set, and are tuned to the coil specifications to eliminate inductive-load related issues. The higher resolution current will provide the ability to actively shield to the level of 1 nT, which is the estimated requirement for the nEDM experiment at TRIUMF.

Bibliography

[1] K.H. Ang, G.C.Y. Chong, and Y. Li. PID control system analysis, design, and technology. *IEEE Transactions on Control Systems Technology*, 13(4):559–576, July 2005.

[2] C.A. Baker, D.D. Doyle, P. Geltenbort, K. Green, M.G.D. van der Grinten, et al. An Improved experimental limit on the electric dipole moment of the neutron. *Phys.Rev.Lett.*, 97:131801, 2006.

[3] S.N. Balashov, K. Green, M.G.D. van der Grinten, P.G. Harris, H. Kraus, et al. A Proposal for a cryogenic experiment to measure the neutron electric dipole moment (nEDM). 2007.

[4] O. Baltag, D. Costandache, M. Rau, A. Iftemie, and I. Rau. Dynamic shielding of the magnetic fields. *Advances in Electrical and Computer Engineering*, 10(4):135–142, 2010.

[5] J. Beringer et al. Review of particle physics. *Phys. Rev. D*, 86:010001, Jul 2012.

[6] Laura Botti, Roberto Buffa, Andrea Bertoldi, Davide Bassi, and Leonardo Ricci. Noninvasive system for the simultaneous stabilization and control of magnetic field strength and gradient. *Review of scientific instruments*, 77(3):035103–035103, 2006.

[7] I.M.V. Caminiti, A. Formisano, M.C. Lupoli, and R. Martone. A new approach to design flexible magnetic active shielding. *Magnetics, IEEE Transactions on*, 49(2):791–794, 2013.

[8] Andrew G. Cohen, D.B. Kaplan, and A.E. Nelson. Progress in electroweak baryogenesis. *Ann.Rev.Nucl.Part.Sci.*, 43:27–70, 1993.

[9] C. J. Dedman, R. G. Dall, L. J. Byron, and A. G. Truscott. Active cancellation of stray magnetic fields in a bose-einstein condensation experiment. *Review of Scientific Instruments*, 78(2):024703, 2007.

[10] Dirk Dubbers and Michael G. Schmidt. The neutron and its role in cosmology and particle physics. *Rev. Mod. Phys.*, 83:1111–1171, Oct 2011.

[11] Jonathan Engel, Michael J. Ramsey-Musolf, and U. van Kolck. Electric Dipole Moments of Nucleons, Nuclei, and Atoms: The Standard Model and Beyond. *Prog.Part.Nucl.Phys.*, 71:21–74, 2013.

[12] Glennys R. Farrar and M.E. Shaposhnikov. Baryon asymmetry of the universe in the minimal Standard Model. *Phys.Rev.Lett.*, 70:2833–2836, 1993.

[13] B. Fillipone. nedm physics and technology of the neutron electric dipole moment (edm). *TRIUMF Summer Institute*, 2012.

[14] Arthur H. Firester. Design of square helmholtz coil systems. *Review of Scientific Instruments*, 37(9):1264–1265, 1966.

[15] PG Harris, DJR May, JM Pendlebury, D Shiers, KF Smith, M van der Grinten, CA Baker, K Green, P Iaydjiev, S Ivanov, et al. The neutron edm experiment at the ill. *Nuclear Instruments and Methods in Physics Research Section A: Accelerators, Spectrometers, Detectors and Associated Equipment*, 440(3):479–482, 2000.

[16] B. Hilgenfeld, E. Strahmel, H. Nowak, and J. Haueisen. Active magnetic shielding for biomagnetic measurement using spatial gradient fields. *Physiol. Meas.*, 24:661–660, 2003.

[17] Joseph L Kirschvink. Uniform magnetic fields and double-wrapped coil systems: Improved techniques for the design of bioelectromagnetic experiments. *Bioelectromagnetics*, 13(5):401–411, 1992.

[18] K. Kobayashi, A. Kon, M. Yoshizawa, and Y. Uchikawa. Active magnetic shielding using symmetric magnetic field sensor method. *Magnetics, IEEE Transactions on*, 48(11):4554–4557, 2012.

[19] V. Alan Kostelecky. The Status of CPT. pages 588–600, 1998.

[20] S Kuriki, A Hayashi, and Y Hirata. Hybrid technique for reduction of environmental magnetic field noise. In *Biomag2000, Proceedings of the 12th International Conference on Biomagnetism*, page 957. Citeseer, 2000.

[21] S. Kuriki, A. Hayashi, T. Washio, and M. Fujita. Active compensation in combination with weak passive shielding for magnetocardiographic measurements. *Review of Scientific Instruments*, 73(2):440–445, 2002.

[22] S. K. Lamoreaux and R. Golub. Detailed discussion of a linear electric field frequency shift induced in confined gases by a magnetic field gradient: Implications for neutron electric-dipole-moment experiments. *Phys. Rev. A*, 71:032104, Mar 2005.

[23] A. Mahgoub, I. Sasada, T. Takeda, and M. Shimada. Desktop shielding system. *Magnetics, IEEE Transactions on*, 49(7):4124–4127, 2013.

[24] Russell Mammei. Passive magnetic shielding. https://ucn.triumf.ca/meetings-and-workshops/collaboration-meetings/japan-collaboration-meeting-august-10-12-2013/RussPassiveMagneticShieldingJuly2013CollabMtg.pdf/, July 2013.

[25] Thomas Mannel and Nikolai Uraltsev. Loop-less electric dipole moment of the nucleon in the standard model. *Physical Review D*, 85(9):096002, 2012.

[26] Y. Masuda. Edm review. presentation at KEK in Tsukubam, Japan, Dec 29-30 2012.

[27] David E. Morrissey and Michael J. Ramsey-Musolf. Electroweak baryogenesis. *New J.Phys.*, 14:125003, 2012.

[28] D.E. Morrissey. Fundamental symmetries and cosmology. *TRIUMF Summer Institute*, 2012.

[29] K. Nagashima, I. Sasada, and K. Tashiro. Adaptive compensation of magnetic fields inside an open cylindrical magnetic shield. *Magnetics, IEEE Transactions on*, 39(5):3223–3225, 2003.

[30] H. Nowak, J. Haueisen, M. Ziolkowski, F. Resmer, J. Schuler, and F. Giessler. Active shielding in measurements of dc near biomagnetic fields. In *Engineering in Medicine and Biology Society, 2001. Proceedings of the 23rd Annual International Conference of the IEEE*, volume 4, pages 3277–3280 vol.4, 2001.

[31] R. D. Peccei and Helen R. Quinn. Constraints imposed by CP conservation in the presence of pseudoparticles. *Phys. Rev. D*, 16:1791–1797, Sep 1977.

[32] E. Pierre. Parametric study of nedm experiment. Google document spreadsheet, 2013.

[33] D Platzek and H Nowak. Low-tc magnetometer used for active shielding in the frequency range dc-500 hz in biomagnetic measurements. *Superconductor Science and Technology*, 12(11):940, 1999.

[34] Maxim Pospelov and Adam Ritz. Electric dipole moments as probes of new physics. *Annals Phys.*, 318:119–169, 2005.

[35] D. Richardson R. Golub and S. Lamoreaux. *Ultra-Cold Neutrons*. IOP Publishing Ltd.

[36] Norman F. Ramsey. Resonance transitions induced by perturbations at two or more different frequencies. *Phys. Rev.*, 100:1191–1194, Nov 1955.

[37] Norman F Ramsey. Electric-dipole moments of elementary particles. *Reports on progress in physics*, 45(1):95, 1982.

[38] S. Razmkhah, M.J. Eshraghi, F. Forooghi, F. Sarreshtedari, and M. Fardmanesh. Fundamental mode fluxgate magnetometers for active magnetic shielding. In *Electrical Engineering (ICEE), 2011 19th Iranian Conference on*, pages 1–1, 2011.

[39] F. Resmer, H. Nowak, F. Gieler, and J. Haueisen. Development of an active magnetic screen to allow a biomagnetometer to be used in an unshielded environment. *Supercond. Sci. Technol.*, 17(12):1365–1371, 2004.

[40] Pavel Ripka. Review of fluxgate sensors. *Sensors and Actuators A: Physical*, 33(3):129–141, 1992.

[41] Andrei Dmitrievich Sakharov. Violation of cp invariance, c asymmetry, and baryon asymmetry of the universe. *Physics-Uspekhi*, 34(5):392–393, 1991.

[42] Paul Sarte. Magnetic field characterisation of the meson hall at triumf for ucn-nedm experiment. http://nuclear.uwinnipeg.ca/elog/Magnetic+Fields/77, February 2013.

[43] John A. Shaw. *The PID Control Algorithm How it works, how to tune it, and how to use it, 2nd Edition.*

[44] M. Daum P. Fierlinger D. George R. Henneck Z. Hochman M. Kasprzak K. Kohlik K. Kirch M. Kuzniak G. Kuehne A. Pichlmaier A. Siodmok A. Szelc T. Brys, S. Czekaj and L. Tanner. Magnetic field stabilization for magnetically shielded volumes by external field coils. *Journal of Research of the National Institute of Standards and Technology*, 110:173–178, 2005.

[45] G. 't Hooft. Computation of the quantum effects due to a four-dimensional pseudoparticle. *Phys. Rev. D*, 14:3432–3450, Dec 1976.

Appendix A

Fluxgate magnetometer basics

Fluxgate sensors are solid-state devices used for measuring the magnitude and direction of dc or low-frequency ac magnetic fields. Fluxgate sensors come is several configurations, the ring core type being the most commonly used. The fluxgate sensor used for magnetic field measurements in the active shielding system developed for this thesis is a racetrack fluxgate, which is essentially a modification of the ring core type sensor.

Figure A.1 shows the main components of a ring core fluxgate sensor. The central ring is typically made from an alloy of high magnetic permeability μ, wrapped in two sets of coil windings. The first set of windings, which are wrapped directly around the ring, are known as the drive windings or the excitation coil. The second set of windings are wrapped around the entire ring forming a pick-up, or sense coil. An ac current is driven into the excitation coil inducing a magnetic flux ϕ within the core. This field from the excitation coil causes the core to become magnetically saturated. If the core is thought of as two separate halves, then a the field generated in one half (ϕ_1) will be in the opposite direction as a the field generated in the other half (ϕ_2). If no external magnetic field is present, the two half cores go in and out of saturation simultaneously. The fields generated by the two half cores cancel, and no net change in flux is measured by the pick-up coil. If an external field B_0 is present, it will cause the saturation in each half of the core to vary relative to one another. The fields produced by the half cores no longer cancel and the pick-up coil is subjected to a net flux. The result is an induced voltage in the pick-up coil, which provides a measure of the external field.

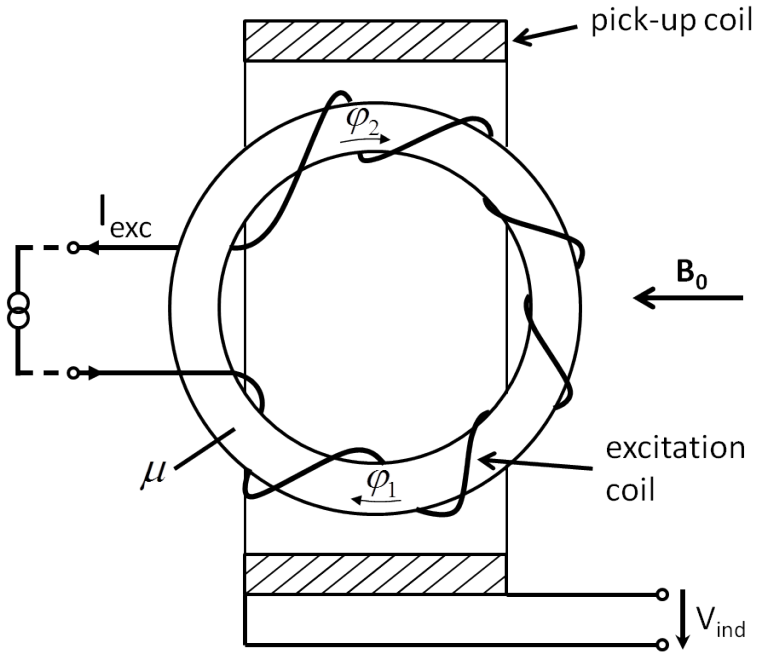

Figure A.1: Ring core fluxgate sensor schematic. The excitation coil is shown wrapped toroidally around the ring core of permeability μ. An ac current I_{exc} is driven into the excitation coil inducing a magnetic field in the core. The bottom half of the core is subject to a flux ϕ_1, and goes in and out of saturation in opposite phase to the top half which is subject to the same flux magnitude in the opposite direction, called ϕ_2. An external magnetic field B_0 causes an imbalance of the saturation in each half of the core, resulting in a net flux through the pick-up coil which induces a measurable voltage that relates to the direction and magnitude of B_0. (Image reproduced by M. Lang from Figure 2 of Reference [40]

The sensor can be placed in a feedback loop (as shown in Figure A.2) in which another coil, known as the compensation or feedback coil, is used to drive the external field to zero resulting in no voltage output from the pick-up coil. The feedback loop maintains the zero voltage output from the pick-up coil by adjusting the current in the feedback coil. The external field measurement is then based on the current driven into the feedback coil. This is known as a feedback magnetometer, and the benefit is an increase in the dynamic range of the fluxgate field measurement [40].

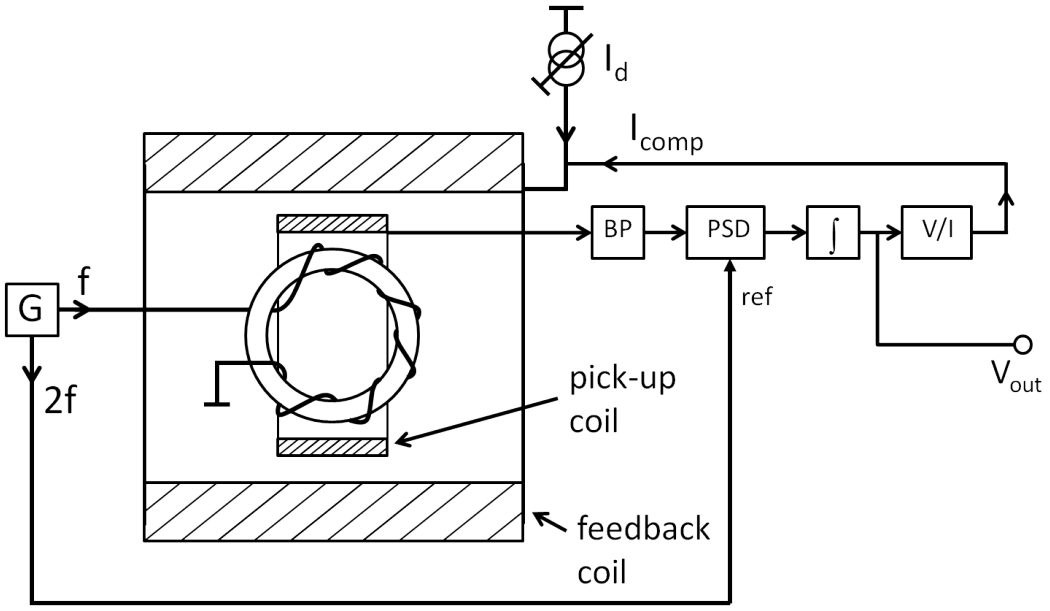

Figure A.2: Schematic of a feedback magnetometer. The excitation coil is driven by a function generator (G). The output of the pick-up coil is band-pass filtered and amplified before passing through a phase sensitive detector (PSD). An integrator is used to filter the ac component and provide amplification for the signal, which is fed back as a compensation current (I_comp) using a voltage-to-current amplifier (V/I). Additional feedback current can be generated by a digitally controlled current source (I_d) which increases the dynamic range of the device. The feedback loop attempts to nullify external magnetic fields by ensuring that the pick-up coil output remains as close to zero as possible, and the feedback voltage is used to measure external magnetic fields. (Image reproduced by M. Lang from Figure 7 of Reference [40]

Appendix B

Hardware specifications

B.1 Bartington Mag-03MSES70 Field Sensor

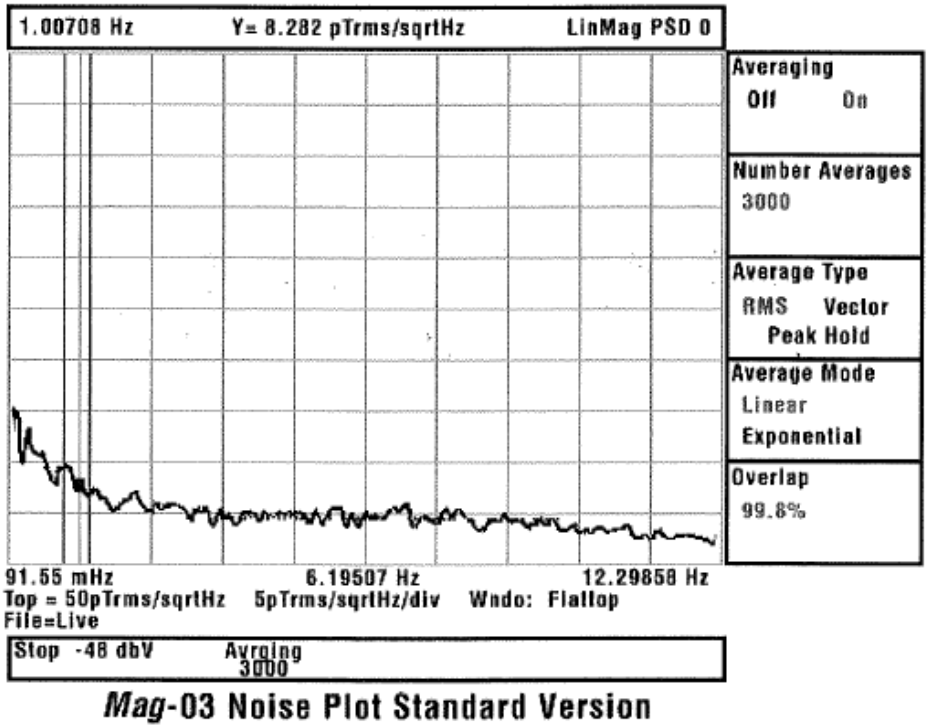

Figure B.1: Bartington calibration plot for Mag-03MSES70, taken from the Bartington operation manual for Mag-03 three-axis magnetic field sensors.

Mag-03 MSES70	Specified Noise	X Cal.	Y Cal.	Z Cal.
Noise at 1 Hz	Standard : 6-10 pTrms/$\sqrt{hz}$	7	6.8	6

Table B.1: Bartington calibration data for Mag-03MSES70 fluxgate used in the system

B.2 Agilent U8002A Power Supply Specifications

Electrical Specifications

Parameter	U8001A	U8002A
Output Ratings (at 0 °C to 40 °C)	0 to +30 V 0 to 3 A	0 to +30 V 0 to 5 A
Line and Load Regulation	CV: <0.01% +2 mV CC: <0.02% +2 mA	
Ripple and Noise (25 °C ±5 °C)	CV: 12 mVp-p, <1 mVrms; CC: 3 mArms	
Load Transient Response Time (within 15 mV from full load to half load and from half load to full load)	<50 µs	
Programming Accuracy[1] (25 °C ±5 °C)	<0.35% +20 mV <0.35% +20 mA	
Readback Accuracy[1] (25 °C ±5 ° C)	<0.35% +20 mV <0.35% +20 mA	
Meter Resolution	Voltage: 10 mV Current: 10 mA	
Maximum Output Float Voltage	±240 Vdc	

Figure B.2: Agilent U8002A power supply specifications.

B.3 Centent CN0122 Amplifier Specifications

ELECTRICAL	MIN.	MAX.	UNIT
Power Supply Voltage	15	32	VDC
Power Supply Current*	--	30	mA
Maximum Load Current	-5	+5	A
Voltage Gain	25.6	28.3	%
Frequency Response	DC	20	kHz
Input Impedance	1M	--	ohms
Input Potentiometer	5K	50K	ohms
Disable Current (Terminal 5, 10V)	--	10	mA
Common Current (Terminal 6, 5V)	--	50	mA
* with no motor connected			
ENVIRONMENTAL	**MIN.**	**MAX.**	**UNIT**
Operating Temperature	-40	+70	°C
	-40	+158	°F
Weight	10.6	14.1	ounce
	300	400	gram
Terminal Screw Torque		4.5	lb/in
DIMENSIONS			**UNIT**
Size (L x W x H)	4.0 x 3.0 x 0.85		inch
	102 x 76 x 22		mm.
Mounting hole centers	3.650 x 2.625		inch
	93 x 67		mm.

Figure B.3: Centent CN0122 dual input motor drive specifications.